

Galactic structure in the outer disk: the field in the line of sight to the intermediate-age open cluster Tombaugh 1¹

Giovanni Carraro^{1,2}

*Dipartimento di Fisica e Astronomia, Università di Padova
Vicolo Osservatorio 3
I-35122, Padova, Italy*

and

Joao Victor Sales Silva^{1,3}

*Observatorio Nacional/MCT
Rua Gen. José Cristino 77
20291-400, Rio de Janeiro, Brazil*

and

Christian Moni Bidin

*Instituto de Astronomia, Universidad Catolica del Norte
Av. Angamos 0610, Casilla 1280
Antofagasta, Chile*

and

Ruben A. Vazquez

*Instituto de Astrofisica de La Plata
CONICET/ UNLP, Paseo del Bosque s/n
La Plata, Argentina*

ABSTRACT

We employ optical photometry and high-resolution spectroscopy to study a field toward the open cluster Tombaugh 1, where we identify a complex population mixture, that we describe in terms of young and old Galactic thin disk. Of particular interest is the spatial distribution of the young population, which consists of dwarfs with spectral

¹ESO, Alonso de Cordoba 3107, Santiago de Chile, Chile

²giovanni.carraro@unipd.it

³Instituto de Astronomia, Universidad Catolica del Norte, Antofagasta, Chile

type as early as B6, and distribute in a *blue plume* feature in the colour-magnitude diagram. For the first time we confirm spectroscopically that most of these stars are early type stars, and not blue stragglers nor halo/thick disk sub-dwarfs. Moreover, they are not evenly distributed along the line of sight, but crowd at heliocentric distances between 6.6 and 8.2 kpc. We compare these results with present-day understanding of the spiral structure of the Galaxy and suggest that they trace the outer arm. This range in distances challenges current Galactic models adopting a disk cut-off at 14 kpc from the Galactic center. The young dwarfs overlap in space with an older component which identifies the old Galactic thin disk. Both young and old populations are confined in space since the disk is warped at the latitude and longitude of Tombaugh 1. The main effects of the warp are that the line of sight intersects the disk and entirely crosses it at the outer arm distance, and that there are no traces of the closer Perseus arm, which would then be either un-important in this sector, or located much closer to the formal Galactic plane. We finally analysed a group of giant stars, which turn out to be located at very different distances, and to possess very different chemical properties, with no obvious relation with the other populations.

Subject headings: editorials, notices — miscellaneous — catalogs — surveys

1. Introduction

Colour-magnitude diagrams (CMD) of stellar fields in the third quadrant of the Milky Way have repeatedly unraveled the remarkable complexity of the stellar populations in the outer Galactic disk. Beyond any reasonable doubt, two dominating features appear on top the main sequence of the nearby Galactic field: a thick main sequence (MS) with a prominent turn off point, and made of intermediate age stars poor in metals, and an almost vertical sequence of young blue stars, popularised as the *blue plume* (Moitinho et al. 2006; Carraro et al. 2005, 2016). This complexity was originally interpreted as the result of the accretion of a satellite onto the Milky Way disk (Martin et al. 2004; Bellazzini et al. 2004), and different age and metallicity sequences described as different episodes of star formation in an individual stellar system, the Canis Major dwarf galaxy.

The *blue plume* deserves particular attention, since up to date no general consensus exists about its nature. This is because in the vast majority of the cases, only photometric data are available, which are not univocal enough to derive solid estimate of the stars' gravity and temperature, and, in turn, to infer their spectral type and distance. Because of the partial leverage of photometric data, various interpretations of the *blue plumes* are available. They can be made of genuine blue young stars, and describe either the last episode of star formation in Canis Mayor (Bellazzini et al.

¹Based on observations carried out at Las Campanas Observatory, Chile (program ID CN009B-042) and Cerro Tololo Inter-American Observatory.

2004), or the structure of the outer Galactic young disk, organised in spiral arms (Carraro et al. 2005; Moitinho et al. 2006; Vazquez et al. 2008). Alternatively, these stars can be the blue straggler population of the old, metal poor population we mentioned before. Finally, they can be mostly hot sub-dwarfs of type O and B, which are known to be present in the general Galactic field, both in the disk and in the halo (Carraro et al. 2015). Obviously, a better scrutiny of these different scenarios can be obtained only via a dedicated spectroscopic study of these blue stars. This is one of the main scope of this work. We focus here on the line of sight toward the loose open cluster Tombaugh 1. To set the scene, we show in Fig. 1 an optical CMD of a 20×20 arcmin field, in the V/V-I plane, derived from a novel set of $UBV(RI)_{KC}$ photometry obtained for the present study. In this CMD we highlight the features we have been discussing so far with four red boxes. Box A encompasses clump stars in the star cluster Tombaugh 1, which we already studied in Sales Silva et al. (2016), and are not relevant for this study. We remind the reader that Tombaugh 1 turned out to be an intermediate age (~ 1 Gy) open cluster, with a metallicity of $[Fe/H] = -0.11 \pm 0.02$, and at 2.6 kpc from the Sun. Boxes B, C, and D are on the other hand central for the present investigation. Box C encompasses a group of blue stars part of the *blue plume* feature. Box D includes stars belonging to a thick blue MS whose turn off point (TO) is located at $V \sim 19$, $(V - I) \sim 0.9$. Finally, box B is composed by a clump of scattered stars, possibly red giant stars belonging to the same stellar population of Box D. The aim of this work is to characterise these three different groups, and establish any possible relation among them. We selected a sample of stars inside each of these boxes and obtain for them high resolution spectroscopy, which we are going to present and analyse in tandem with the broad band optical photometry.

The paper is organised as follows: In Sect. 2 we present the observational material, both photometric and spectroscopic. Section 3 is devoted to the analysis of the various photometry diagrams, and the derivation of blue plume star individual reddening and distance. A detailed discussion of the spectroscopic data is performed in Section. 4, and in Section 5 we focus on the results of the abundance analysis of box B stars. The discussion of our results, and the conclusions of this work are provided in Section 6.

2. Observations and data reduction

2.1. Photometry

The region of interest has been observed with the Y4KCAM camera attached to the 1.0m telescope, which is operated by the SMARTS consortium² and located at Cerro Tololo Inter-American Observatory (CTIO). This camera is equipped with an STA 4064 \times 4064 CCD with 15- μ pixels, yielding a scale of 0.289"/pixel and a field-of-view (FOV) of $20' \times 20'$ at the Cassegrain focus of

²<http://http://www.astro.yale.edu/smarts>

the CTIO 1.0m telescope. The CCD was operated without binning, at a nominal gain of 1.44 e⁻/ADU, implying a readout noise of 7 e⁻ per quadrant (this detector is read by means of four different amplifiers)³. As an illustration we show a V-band frame in Fig. 2.

The observational data were acquired on the night of January 30, 2008, as summarised in Table 1. We observed Landolt’s SA 98 *UBV(RI)_{KC}* standard stars area (Landolt 1992, see Table 1), to tie our *UBVRI* instrumental system to the standard system. The average seeing was 1.0″.

Our *UBVRI* instrumental photometric system was defined by the use of a standard broadband Kitt Peak *BVR_{kc}I_{kc}* set in combination with a U+CuSO₄ *U*-band filter⁴. To determine the transformation from our instrumental system to the standard Johnson-Kron-Cousins system, we observed 46 stars in area SA 98 (Landolt 1992) multiple times, and with different air-masses ranging from ~1.2 to ~2.3. Field SA 98 is very advantageous, as it includes a large number of well observed standard stars, and it is completely covered by the CCD’s FOV. Furthermore, the standard’s color coverage is very good, being: $-0.5 \leq (U-B) \leq 2.2$; $-0.2 \leq (B-V) \leq 2.2$ and $-0.1 \leq (V-I) \leq 6.0$.

2.1.1. Data Reduction

Basic calibration of the CCD frames was done using the IRAF⁵ package CCDRED. For this purpose, zero-exposure frames and twilight sky flats were acquired every night. Photometry was then performed using the IRAF DAOPHOT and PHOTCAL packages. Instrumental magnitudes were extracted following the point spread function (PSF) method (Stetson 1987). A quadratic, spatially variable, master PSF (PENNY function) was adopted. The PSF photometry was finally aperture-corrected, filter by filter. Aperture corrections were determined by performing aperture photometry for a suitable number (typically 20 to 40) of bright stars selected across the whole field. These corrections were found to vary between 0.105 and 0.315 mag, depending on the filter.

³QE and other detector characteristics can be found at: <http://www.astronomy.ohio-state.edu/Y4KCam/detector.html>

⁴Transmission curves for these filters can be found at <http://www.astronomy.ohio-state.edu/Y4KCam/filters.html>

⁵IRAF is distributed by the National Optical Astronomy Observatory, which is operated by the Association of Universities for Research in Astronomy, Inc., under cooperative agreement with the National Science Foundation.

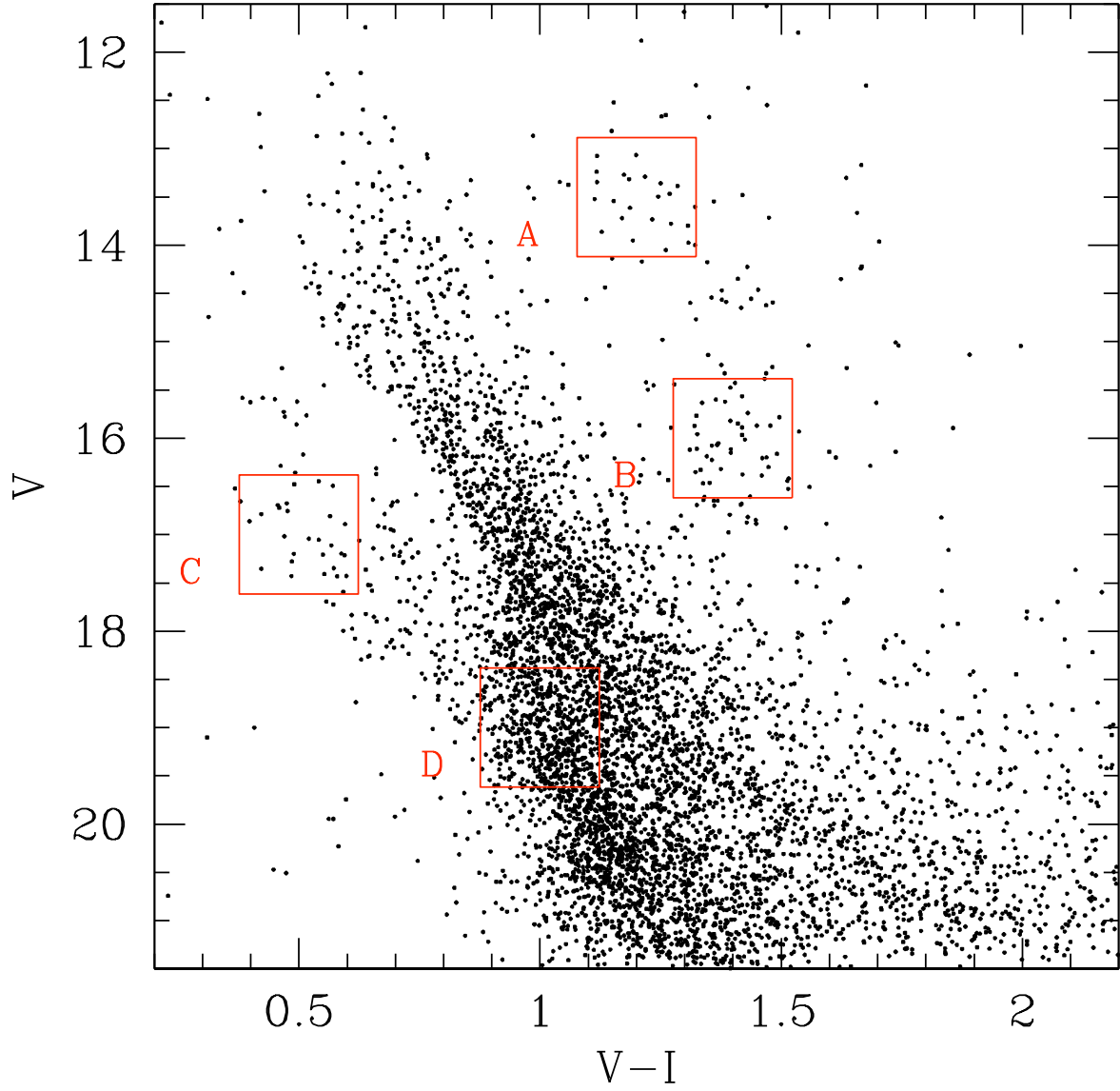


Fig. 1.— A color-magnitude diagram of the region under study, with highlighted the areas where spectroscopy has been conducted.

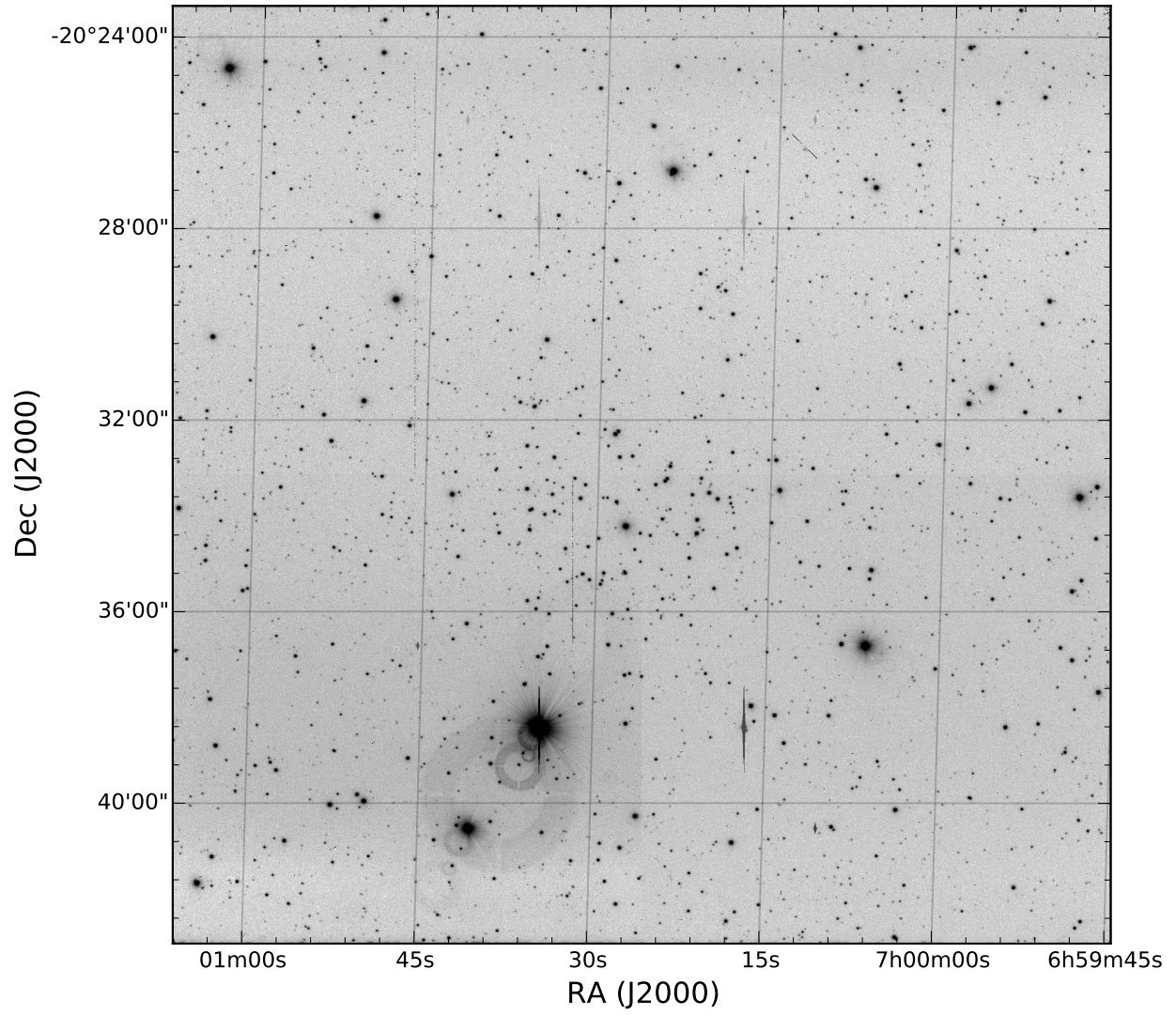


Fig. 2.— A 900 secs V band frame of the area covered by this study.

2.1.2. Final photometry

Our final photometric catalogs consist of 3275 entries with $UBV(RI)_{KC}$ measurements down to $V \sim 22$ for Tombaugh 1. Many more entries are available when we include stars not having U magnitude.

After removing both saturated stars and stars having only a few measurements in the catalog of Landolt (1992), our photometric solutions for a grand total of 183 measurements in U and B , and of 206 measurements in V , R and I , are given by:

$$\begin{aligned}
 U &= u + (3.279 \pm 0.010) + (0.47 \pm 0.01) \times X - (0.030 \pm 0.016) \times (U - B) \\
 B &= b + (2.033 \pm 0.012) + (0.29 \pm 0.01) \times X - (0.110 \pm 0.012) \times (B - V) \\
 V &= v + (1.673 \pm 0.007) + (0.16 \pm 0.01) \times X + (0.022 \pm 0.007) \times (B - V) \\
 R &= r + (2.768 \pm 0.007) + (0.10 \pm 0.01) \times X + (0.053 \pm 0.007) \times (V - R) \\
 I &= i + (2.674 \pm 0.011) + (0.08 \pm 0.01) \times X + (0.048 \pm 0.008) \times (V - I)
 \end{aligned}$$

The final *r.m.s* of the fitting was 0.073, 0.069, 0.035, 0.030, and 0.030 in U , B , V , R and I .

Global photometric errors were estimated using the scheme developed by Patat & Carraro (2001, Appendix A1), which takes into account the errors in the PSF fitting procedure (i.e. from ALLSTAR), and the calibration errors (corresponding to the zero point, color terms, and extinction errors). In Fig. 3 we present the global photometric error trends plotted as a function of V magnitude. Quick inspection indicates that stars brighter than $V \approx 21$ mag have errors much lower than 0.10 mag both in color and in magnitude, apart from the $(U - B)$ color.

2.2. Astrometry

For approximately three-hundred stars in our photometric catalog J2000.0 equatorial coordinates are available from the Guide Star Catalogue⁶, version 2 (GSC-2.2, 2001). Using the SkyCat tool at ESO and the IRAF tasks *ccxymatch* and *ccmap*, we first established a transformation between our (X, Y) pixel coordinates (from ALLSTAR) and the International Celestial Reference Frame. These transformations have an *r.m.s.* value of typically $0.15''$. Finally, using the IRAF task *cctran*, we computed J2000.0 coordinates for all objects in our catalog.

⁶Space telescope Science Institute, 2001, The Guide Star Catalogue Version 2.2.02.

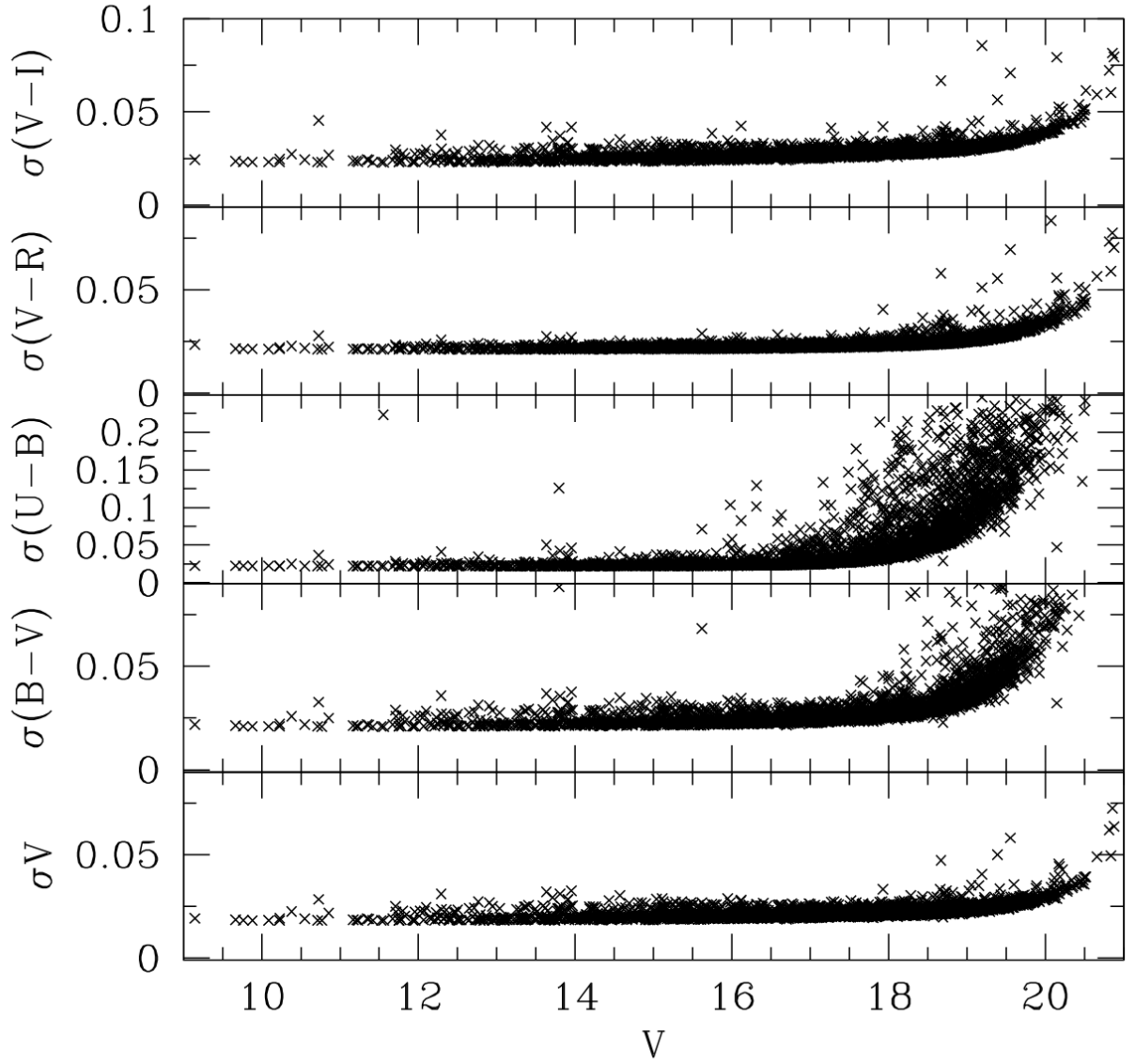


Fig. 3.— Trends of global photometric errors in color and magnitude as a function of the V mag.

2.3. Spectroscopy

During the nights of 2010 January 5, 6, 9 and 10, we observed 40 stars of the field towards the open cluster Tombaugh 1 (10 stars from box A and B, 11 stars from box C and 9 stars from box D, see Fig. 1 on Cerro Manqui at the Las Campanas Observatory using the *Inamori-Magellan Areal Camera & Spectrograph* (IMACS, Dressler et al. 2006), attached to the 6.5m Magellan Telescope. The ten potential cluster stars of box A were studied in Sales Silva et al. (2016). For the stars of boxes A, B and C, we used the multi-object echelle (MOE) spectroscopic mode, while the spectra of the box D stars were obtained using the multi-object mode with the grating 600 lines/mm (G600-8.6). The spectra have a resolution of $R \approx 20000$ and $R \approx 5260$ in case of the MOE and G600 mode, respectively. In both spectroscopic modes the wavelength ranges of stellar spectra vary according to the position of the star in the observation mask, but usually it goes from 4200 Å to 9100 Å for the MOE mode, while for the G600 mode the range is from 3650 Å to 6750 Å. The IMACS detector is a mosaic of eight CCDs with gaps of 0.93mm between them, causing small gaps in stellar spectra. The exposure times for the stars of the boxes B, C and D were 9000s, 14400s and 6300s, divided in 3, 4 and 2 exposures, respectively. Table 2 gives some information about the observed stars: identification (IDs), equatorial coordinates, V and $(V - I)$ from our photometry, and spectral signal-to-noise (S/N) at 6000 Å. The identification system for all stars analysed in this work refers to identification of stars in our photometry. The nominal S/N ratio was evaluated by measuring with IRAF the *rms* flux fluctuation in selected continuum windows.

The reduction of the spectra was performed in a standard manner under IRAF as described in details in Sales Silva et al. (2016). The eight CCDs were de-biased and flat-fielded separately with the task *ccdproc*, combined in a single frame with *imcreate* and *imcopy*, then the spectra were optimum-extracted (Horne 1986) with *doecslit* (*doslit* for G600 mode), sky-subtracted with *background*, and wavelength calibrated with *ecidentify* (*identify* for the G600 spectra). The cosmic rays were removed with the IRAF Laplacian edge-detection routine (van Dokkum 2001).

3. Photometric diagrams

We start deriving some insights on the properties of the stellar population in the line of sight to Tombaugh 1 by inspecting a suite of photometric diagrams. Inspection of the CMDs of all the stars in the field of view in Fig. 4 reveals three prominent features: (1) a cluster MS with a TO at $B \sim 14.5$ ($V \sim 18.5$) and a handful of scattered red clump stars at $B \sim 14.3$ ($V \sim 14.2$) and $(B-R) \sim 1.2$, which we discussed in Sales Silva et al. (2016); (2) a second, thick, well-populated MS with a TO at $B \sim 19.5$ that looks like the MS of an intermediate-age/old stellar population; and (3) a scattered plume of blue stars, in the magnitude range 16–19 that resembles a young stellar population. The last feature is very similar to the *blue plumes* found in the directions of other clusters (Carraro et al. 2016, and references therein) in the third Galactic quadrant.

Table 1: Log of *UBVRI* photometric observations.

Target	Date	Filter	Exposure (sec)	airmass
Tombaugh 1	30 January 2008	U	10,20,100,200,600,1500	1.28–1.52
		B	5,10,100,200,1600,1500	1.15–1.20
		V	5,10,60,120,600,1200	1.01–1.21
		R	3x5,10,60,120,600,1200	1.02–1.15
		I	5,4x10,100,200,600,1200	1.03–1.24
SA 98	30 January 2008	U	2x10,200,2x400	1.15–2.21
		B	10,100,2x200	1.15–2.36
		V	10,50,2x100	1.16–2.53
		R	10,50,2x100	1.17–2.61
		I	10,50,2x100	1.16–2.46

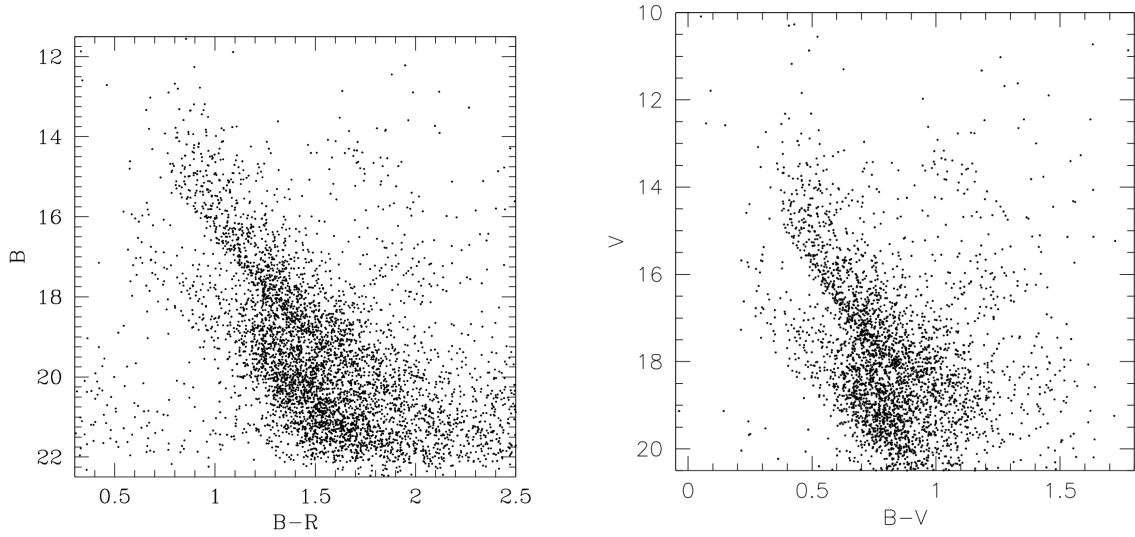


Fig. 4.— CMDs of the stars in the line of sight to the star cluster Tombaugh 1. In the right panel, the CMD has been constructed using stars having simultaneous measures in U, B, and V only, to make easier the interpretation of Fig. 5.

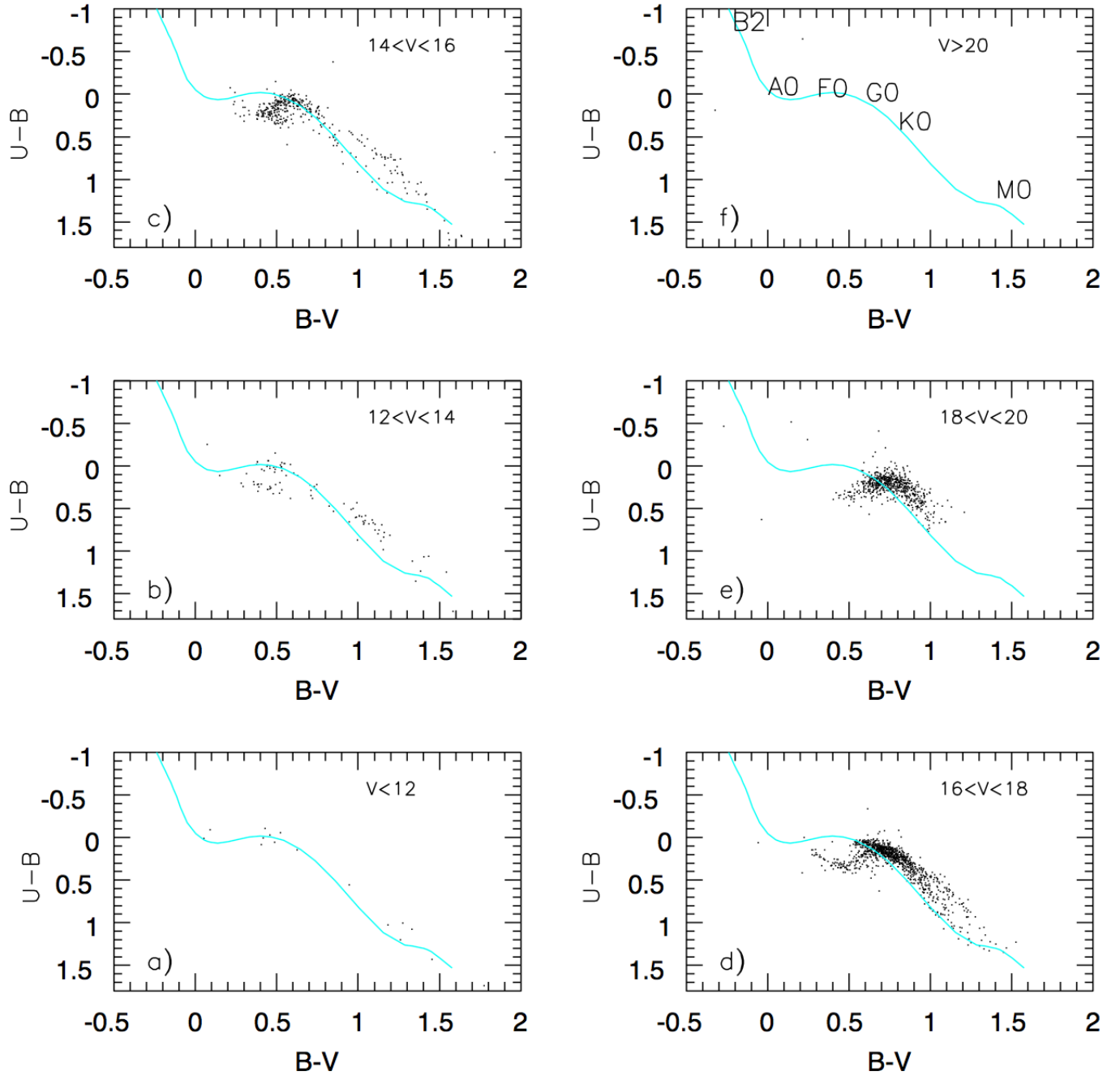


Fig. 5.— The TCDs of the stars in the line of sight to the star cluster Tombaugh 1 extracted from the CMD (right panel of Fig. 4), by binning in magnitude. Only stars having U, B, and V measures simultaneously are plotted.

As amply discussed in Carraro et al. (2016) it is quite straightforward to characterise the *blue plume*, since it would be composed of supposedly young stars for which a robust handling of their properties is possible with UBV photometry. We start discussing more in detail the CMD, by plotting stars in different magnitude bins in the classical two-colour diagram (TCD) U-B/B-V, as shown in Fig. 5. A synoptic view of Fig. 4 and Fig. 5 helps the various CMD components to emerge more clearly, as we already illustrated in the past (see, e.g., Carraro et al. 2010). In the various panels the cyan line is an empirical zero reddening, zero-age main sequence (ZAMS) from Turner (1976,1979). The TCD for $V \leq 12$ (lower left panel) only shows a few zero reddening stars of different spectral type (from A0 to F-G and M) located close to the Sun. The middle-left panel is surely more interesting, since on top the clump of nearby un-reddened F-G stars, it shows two groups of reddened stars (spectral type A and K-M) clearly belonging to the star cluster Tombaugh 1, the first indicating the cluster TO, and the second the red giant clump. The upper-left panel is sampling Tombaugh 1 TO and MS, but also shows a few giant stars, both reddened and un-reddened. The next panel (lower-right) is by far the most intriguing. One can readily notice an important sequence of early type, reddened stars, totally absent in the previous TCDs, which runs from approximately mid B spectral type all the way to K-M. One can also notice (at $(B - V) \sim 0.5$), $(U - B) \sim 0.0$) a somewhat detached, truncated, less reddened, sequence. This latter is, again, Tombaugh 1 MS, while the more reddened sequence samples the *blue plume* up to spectral type A0, and later starts to sample the thick blue MS whose TO is at $(B-V) \sim 0.8$. This can be appreciated by the density increase of stars about this color in the TCD. Besides, also the giant sequence is dual, and contain zero reddening nearby giants, and more distant, reddened giants, possibly associated with the blue thick MS we just described. Finally, the middle-right panel only shows stars in the dominant thick blue MS. The last, top-right, panel is only used to indicate the approximate location of different spectral type stars.

We focus now on the lower right panel, and attempt at deriving the properties of the stars which populated the early spectral type branch, and correspond to the *blue plume*. We obtain a reddening solution for these stars using the TCD in the standard way. This is illustrated in Fig. 6.

The reddening law in the third Galactic quadrant has been recently debated in the literature. As discussed in Carraro et al. (2016) and earlier by Moitinho (2001) and Turner (1976) the reddening law in the third Galactic quadrant seems to deviate from the normal one, namely it is not described by the standard value of 3.1 for $R_V = \frac{A_V}{E(B-V)}$. A value of $R_V=2.9$ would be more appropriate for this Galactic sector. This is certainly true for Tombaugh 1 line of sight, as discussed by Turner (1983). Although the level of deviation from the normal law is not large, we prefer to adopt 2.9 in the following.

The solid black line in Fig. 6 is a zero reddening, zero age MS, while the two red lines are the same ZAMS, but shifted by $E(B - V) = 0.3$ and 0.7 along the reddening line, which is indicated by the red arrow in the top-right corner of the plot. The two reddened ZAMS bracket the *blue plume* stars, which therefore exhibit a mean reddening $E(B - V)=0.5 \pm 0.2$, indicating a significant

amount of variable reddening. We now analyse the reddening distribution of this population by deriving individual stars' reddening.

To determine reddenings, spectral types and, eventually, distances we then proceed as follows. First we derive intrinsic colours using the two relationships:

$$E(U - B) = 0.76 \times E(B - V), \quad (1)$$

and

$$(U - B)_0 = 3.69 \times (B - V)_0 + 0.03. \quad (2)$$

The intrinsic color $(B-V)_0$ is the positive root of the second order equation one derives by combining the above expressions. Intrinsic colours $((U-B)_0$ and $(B-V)_0$) are then directly correlated to spectral type, as compiled for instance by Turner (1976,1979). The solution of the equations above therefore allows us to encounter stars having spectral types earlier than A0.5. For these stars we know the absolute magnitude M_V and, from the apparent extinction-corrected magnitude V_0 , we finally infer the photometric distance.

Starting from the general equation for the distance:

$$(m - M)_o = (m - M)_V - A_V = 5 \times \log(Dist) - 5 \quad (3)$$

errors in distances are computed as follows:

$$\Delta (Dist) = \ln(10) \times Dist \times \Delta [\log(Dist)];$$

$$\Delta [\log(Dist)] = \frac{1}{5} \times \Delta V + \Delta (M_V) + \Delta (A_V);$$

$$\Delta (M_V) = 0;$$

$$\Delta (A_V) = 2.9 \times \Delta (B-V);$$

$\Delta (V)$ and $\Delta(B-V)$ directly comes from photometry; finally

$$\Delta (Dist) = \ln(10) \times Dist \times 1/5 \times [\Delta V + 2.9 \times \Delta (B-V)]$$

The reddening distribution is shown in the left panel of Fig. 7. It is quite broad, and peaks at $E(B-V) \sim 0.5$. A gaussian fit yields the value $E(B-V) = 0.55 \pm 0.20$. On the right panel of the same figure we show the distribution of the absolute distance moduli for the same stars. Most stars are

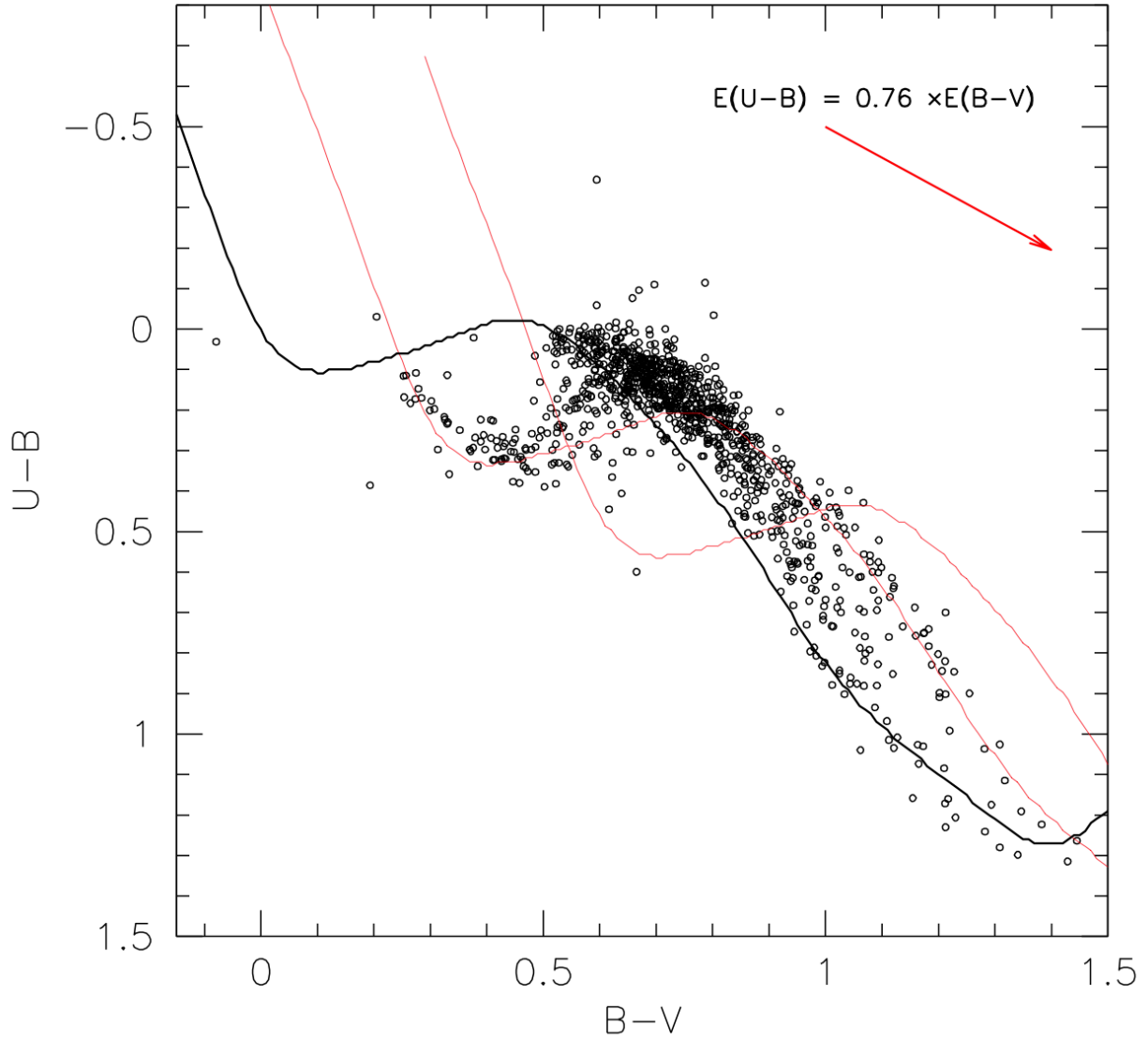


Fig. 6.— TCDs of the stars in the line of sight to the star cluster Tombaugh 1, and in the magnitude range $16 \leq V \leq 18$. The solid line is a zero reddening, zero age main sequence, while the two red lines encompassing the early type stars are the very same ZAMS, but displaced by 0.4 and 0.6 mag along the reddening vector.

located in the range $14.0 \leq (m - M)_0 \leq 15.5$, which implies a distance range $6.3 \leq d_{\odot} \leq 10.0$ kpc. Errors in distances as computed using the formulae described above, are 0.5 kpc for the closer stars, and up to 1.5 kpc for the most distant stars. We notice, finally, a group of very distance stars, at $(m - M)_0 \sim 16$, whose distance would be as large as 19 ± 3.5 kpc. We will return to this group later.

4. Spectroscopic analysis

4.1. Radial velocities

The radial velocity (RV) of the targets were measured on each single exposure independently. We thus checked for RV variations, and shifted them to laboratory wavelengths before co-adding the spectra of each star. The zero-point offset of each spectrum was estimated using the *fxcor* IRAF task, by cross-correlating (Tonry & Davis 1979) the observed telluric band at 6800 Å with that of a FEROS high-resolution solar spectrum collected by us in a previous run (Moni Bidin et al. 2012a). The heliocentric correction was estimated through the *rvcorrect* task, and applied to each measurement. The final RV of each star was obtained from the weighted mean of the single epochs. Our results are given in Table 3.

For box B stars, the line-to-line differences between the observed and laboratory wavelengths of the unblended Fe lines were used to determine the target RV. The final error was assumed as the largest difference between the three heliocentric radial velocity values multiplied by 0.59 (small sample statistics, see Keeping 1962). The RV of box C stars was estimated by cross-correlating the H $_{\alpha}$ line with the synthetic template of a 10 000 K MS star taken from the Munari et al. (2005) library. Previous works have shown that the results of cross-correlation are not affected by the exact choice of the template, and a marginal mismatch between object and template spectral types only enhances the formal uncertainties (Morse et al. 1991; Moni Bidin et al. 2011). When other strong features were visible in the spectral range, such as the H $_{\beta}$ line, we verified that they returned identical results within errors. However, as the availability of these features varied among the targets, for the sake of consistency we used only the H $_{\alpha}$ line to derive the final results. The same procedure was adopted for box D stars, except that the aforementioned FEROS Solar spectrum was used as template.

4.2. Box B: stellar parameters and chemical abundances

The lines list used to determine the chemical abundance of Na, Al, Mg, Si, Ca, Ti, Cr, Fe and Ni is the same we used recently in Sales Silva et al. (2016). In Tables 6 and 7 we show our lines list with excitation potential (χ) and oscillator strength (gf) for all absorption lines analysed in this work. The values of the oscillator strength adopted for the Fe I and Fe II lines were taken from

Table 2: Fundamental information for the spectroscopically observed stars.

Box B					
ID	RA(2000.0)	DEC(2000.0)	V	$(V - I)$	S/N
	degree	degree	mag	mag	
11029	105.0619584	-20.5959712	15.97	1.446	65
13540	105.0867260	-20.6172278	16.25	1.393	60
13964	105.0912208	-20.6830230	16.48	1.457	35
15490	105.1050867	-20.4189783	16.06	1.324	35
26606	105.1789665	-20.4134974	15.83	1.428	35
27955	105.1880177	-20.5694871	15.72	1.381	75
28064	105.1887938	-20.4728788	15.57	1.392	60
29403	105.1989331	-20.6387084	16.62	1.512	20
31364	105.2138666	-20.6505511	15.96	1.475	60
32782	105.2261239	-20.4283761	16.06	1.416	35
35658	105.2524590	-20.4933638	16.30	1.458	35
Box C					
6507	105.0154684	-20.7188840	17.31	0.549	20
8542	105.0351681	-20.4324223	17.21	0.566	10
9227	105.0426156	-20.4693299	16.82	0.458	20
12018	105.0719883	-20.4367526	16.46	0.491	15
13279	105.0840465	-20.4816043	16.88	0.676	20
16940	105.1177477	-20.5710991	17.24	0.653	20
24772	105.1683352	-20.4800548	16.77	0.474	15
28816	105.1943277	-20.5676972	16.58	0.489	25
30971	105.2109730	-20.6079883	17.06	0.695	25
31183	105.2125614	-20.5339462	17.30	0.696	15
32089	105.2197018	-20.6357812	16.41	0.659	40
Box D					
7421	105.0244349	-20.5505733	19.37	1.052	15
9011	105.0398536	-20.6999266	18.65	0.986	20
9834	105.0492119	-20.4859526	19.38	1.044	10
11923	105.0711463	-20.4358597	19.10	0.942	10
19341	105.1359171	-20.4658181	19.36	1.045	10
22319	105.1533307	-20.5625042	18.88	1.004	20
23667	105.1614867	-20.4377257	18.46	0.966	15
36132	105.2567499	-20.4139628	18.54	0.986	10
31274	105.2133773	-20.5128144	19.38	1.057	10

Lambert et al. (1996) and Castro et al. (1997). The references of the atomic parameters for the other absorption lines are shown in Table 7.

The chemical abundance of Na, Al, Mg, Si, Ca, Ti, Cr and Ni for the red clump stars (box B) were obtained through the equivalent widths (EWs) of the absorption lines corresponding to each element. The EWs were measured using the task *splot* in IRAF by fitting the observed absorption line with a Gaussian profile. Absorption lines with EWs greater than 160 mÅ are saturated and were rejected in our analysis due to the impossibility to fit a Gaussian profile to these lines (Pereira et al. 2011). The EWs used to derive the chemical abundance are shown in Tables 6 and 7.

The local thermodynamic equilibrium (LTE) model atmospheres of Kurucz (1993) and the spectral analysis code MOOG (Snedden 1973) were used to determine the chemical abundances and atmospheric parameters for the stars of box B. The effective temperature, surface gravity and micro-turbulence velocity were derived using measurements of EWs for a set of Fe I and Fe II lines shown in Table 6. The unique solution for the effective temperature, surface gravity and micro-turbulence velocity was obtained simultaneously under the approximations of excitation and ionisation equilibrium, and independence between the Fe abundance and reduced EW. The effective temperature was set through the excitation equilibrium determined by zero slope of the trend between the iron abundance derived from Fe I lines and the excitation potential of the measured lines. The micro-turbulence velocity was adjusted until both the strong and weak Fe I lines gave the same abundance. And the ionisation equilibrium was used to derive the surface gravity, and was defined by the equality of the abundances of Fe I and Fe II.

Uncertainties in the effective temperature and micro-turbulence velocity were inferred from the uncertainties in the slopes of the FeI abundances versus potential excitation and abundance of Fe I versus reduced EW, respectively. On the other hand, the uncertainty in the surface gravity was obtained by varying this parameter iteratively around the first guess value until surface gravity was obtained, that changes the abundance of Fe II by exactly one standard deviation of the $[FeI/H]$ mean value. In Table 3 we show the atmospheric parameters and their respective uncertainties for the red clump stars.

The atmospheric parameters for the stars #15490, #29403 and #35658 were not determined because the spectra of these stars have low S/N. Despite the low S/N also shown by the spectrum of star #13964 and #32782, we could derive the atmospheric parameters for but with large uncertainty (see Table 3). In the analysis of the star #26606, we faced a problem in obtaining the micro-turbulence velocity due to the low number of absorption lines with small EW, causing again considerable uncertainty in the atmospheric parameters.

In Table 4 we show the abundance ratios ($[X/Fe]$) for Na, Al, Mg, Ca, Si, Ti, Cr and Ni for the red clump stars. Our chemical abundances were normalised to the solar abundances obtained through a high-resolution FEROS solar spectrum (Moni Bidin et al. 2012a). In Table 8 we list our solar abundances compared to solar abundance of Grevesse & Sauval (1998) and Asplund et al. (2009). The total uncertainty of the abundances for the red clump stars are shown in Table 5.

The uncertainties of the chemical abundance associated to the errors of the effective temperature, micro-turbulence velocity and surface gravity were calculated independently, and then quadratically combined to provide the global abundance uncertainty.

4.3. Box C and D: stellar parameters

The temperature, gravity, and rotational velocity of Box C stars were measured by fitting the H_α and H_β Balmer lines and the 4922 Å He I feature with synthetic spectra, as done in Majaess et al. (2013) for similar MS stars. To this aim, we employed the *fitprof21* code, developed by Bergeron et al. (1992) and Saffer et al. (1994), and subsequently modified by Napiwotzki et al. (1999). The routine was fed with a grid of solar-metallicity LTE model spectra ($T_{\text{eff}}=8000\text{--}30000$ K, $\log g=3.5\text{--}5.0$ dex) generated from ATLAS9 (Kurucz 1993) model atmospheres through the Lemkes version⁷ of the LINFOR program (developed originally by Holweger, Steffen, and Steenbock at Kiel University). In fact, deviations from LTE have negligible effects on the Balmer and He lines at the temperatures of program stars (Nieva & Przybilla 2007). The routine determines the best-fit parameters through a χ^2 minimisation statistics. Extensive details about the synthetic spectra fitting procedure can be found in Moni Bidin et al. (2012b).

While the method ideally works when the whole Balmer series can be simultaneously fit, a minimum of two features is required to avoid the degeneracy between temperature and gravity. In our case, the profile of the only He line could constrain the rotational velocity and, to a limited extent, the temperature, but the two Balmer lines were needed for a reliable determination of T_{eff} and $\log g$. This was not possible for three targets, where H_β line did not fall in the spectral range. We could still obtain a good fit of the single H_α line for the stars #6507 and #8542, although the larger errors reflect the high uncertainty of the measurements. For star #12018, on the contrary, we had to assume $\log g=4.2$, as typical of a MS star, and adopt only the temperature as fit parameter.

The strength of Balmer lines has a maximum at ≈ 10000 K, and it declines both for hotter and cooler stars. The temperatures obtained by one Balmer line only could thus present two acceptable

⁷<http://a400.sternwarte.uni-erlangen.de/ai26/linfit/linfor.html>

Table 3: Atmospheric parameters from spectroscopy of stars of box B.

ID	T_{eff} (K)	$\log g$ (dex)	ξ km s^{-1}	[FeI/H] $\pm\sigma$ (#)	[FeII/H] $\pm\sigma$ (#)	$\langle RV \rangle$ (km s^{-1})	$E(V-I)$	$(V-Mv)_0$	d (pc)
11029	5250 \pm 200	3.3 \pm 0.2	2.2 \pm 0.4	-0.03 \pm 0.13(43)	-0.03 \pm 0.12(8)	76.2 \pm 1.4	0.53 \pm 0.19	12.41 \pm 0.61	3000 \pm 900
13540	5300 \pm 200	3.1 \pm 0.2	1.8 \pm 0.3	0.03 \pm 0.14(27)	0.05 \pm 0.07(3)	74.6 \pm 1.8	0.56 \pm 0.11	13.62 \pm 0.80	5300 \pm 2000
13964 ^a	4700 \pm 300	2.0 \pm 0.4	2.5 \pm 0.6	-0.68 \pm 0.18(23)	-0.70 \pm 0.18(3)	73.9 \pm 2.1	0.39 \pm 0.19	16.55 \pm 1.17	20500 \pm 11600
26606 ^b	4600 \pm 450	2.7 \pm 0.5	2.5 \pm 1.0	-0.46 \pm 0.34(19)	-0.45 \pm 0.26(3)	28.1 \pm 3.6	0.30 \pm 0.25	13.04 \pm 1.09	4000 \pm 2100
27955	5250 \pm 250	3.8 \pm 0.2	2.2 \pm 0.4	-0.24 \pm 0.15(35)	-0.24 \pm 0.08(6)	116.5 \pm 1.3	0.53 \pm 0.10	10.46 \pm 0.57	1200 \pm 300
28064	4700 \pm 150	2.1 \pm 0.3	2.3 \pm 0.4	-0.58 \pm 0.14(33)	-0.57 \pm 0.15(5)	68.0 \pm 3.2	0.37 \pm 0.15	15.45 \pm 0.89	12300 \pm 5200
31364	5050 \pm 150	2.0 \pm 0.2	1.5 \pm 0.3	-0.24 \pm 0.13(31)	-0.23 \pm 0.08(3)	65.6 \pm 0.3	0.44 \pm 0.09	16.81 \pm 0.90	23000 \pm 980
32782	5000 \pm 250	3.1 \pm 0.3	3.0 \pm 0.6	-0.39 \pm 0.13(16)	-0.41(1)	0.9 \pm 3.0	0.49 \pm 0.14	12.79 \pm 0.48	3600 \pm 800

Notes. For [Fe I/H] and [Fe II/H], we also show the standard deviation and the number of lines (#) employed. a: Large uncertainty in the atmospheric parameters and metallicity of this star due to low S/N. b: Problem in obtaining of micro-turbulent velocity (ξ) due to the low number of absorption lines with small equivalent width causing considerable uncertainty in the metallicity.

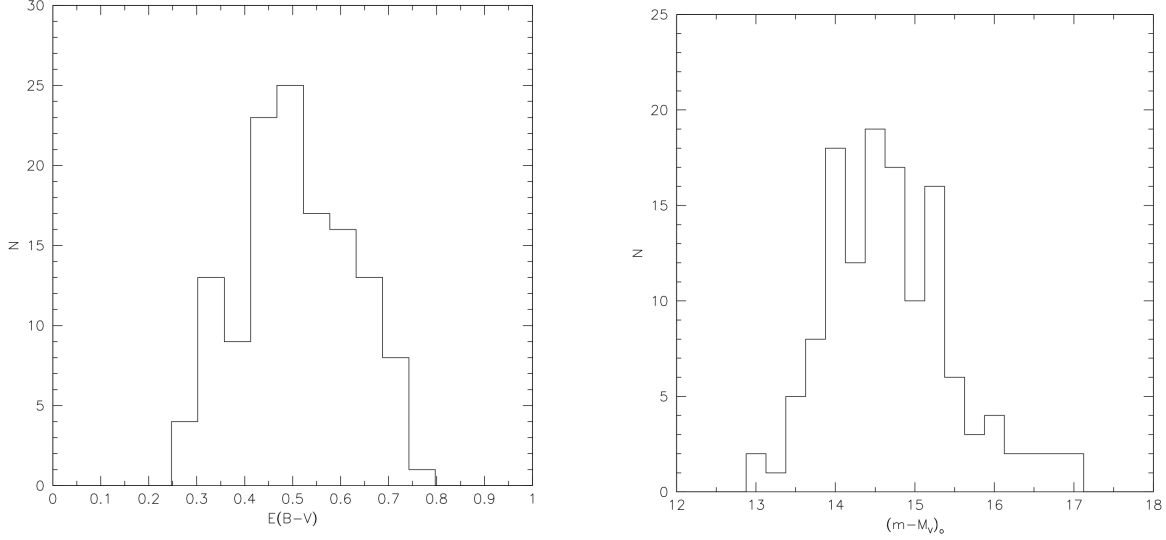


Fig. 7.— Distribution of individual star reddenings (left panel) and reddening corrected distance moduli (right panel).

Table 4: Abundance Ratios ($[X/Fe]$) for the elements from Na to Cr for the stars from box B.

ID	Box B							
	[Na/Fe]NLTE	[Mg/Fe]	[Al/Fe]	[Si/Fe]	[Ca/Fe]	[Ti/Fe]	[Cr/Fe]	[Ni/Fe]
11029	+0.19(1)	+0.18(1)	—	+0.13±0.05(2)	-0.20±0.12(4)	+0.29±0.10(5)	-0.09±0.02(3)	-0.08±0.09(10)
13540	+0.27±0.01(2)	—	+0.14±0.04(2)	+0.12±0.16(3)	+0.18±0.11(3)	+0.29±0.04(3)	-0.21±0.10(3)	+0.08±0.13(10)
13964	+0.40(1)	+0.66(1)	+0.37±0.01(2)	—	+0.47±0.07(4)	+0.21±0.14(6)	+0.35(1)	+0.24±0.14(4)
26606	—	+0.41±0.06(2)	+0.47(1)	+0.54(1)	—	+0.23±0.03(2)	+0.12(1)	+0.01(1)
27955	—	+0.00±0.13(2)	—	+0.11±0.10(2)	-0.17±0.17(4)	+0.37±0.08(5)	-0.11±0.03(3)	+0.17±0.16(11)
28064	+0.38(1)	+0.24±0.08(2)	+0.10±0.11(4)	+0.12(1)	-0.30±0.03(2)	+0.22±0.13(4)	+0.10±0.13(2)	-0.22±0.07(7)
31364	+0.37(1)	-0.21±0.10(2)	—	+0.07±0.17(3)	+0.03±0.11(3)	+0.31±0.15(3)	+0.07±0.02(2)	-0.11±0.16(10)
32782	+0.42(1)	+0.67(1)	+0.59(1)	—	—	+0.54±0.14(3)	+0.10(1)	-0.02±0.15(5)

Notes. For all abundances ratios, we also show the standard deviation and the number of lines employed. [Na/Fe] accounts for the NLTE effects calculated as in Gratton et al. (1999), see text.

Table 5: Abundance uncertainties for star from box B.

11029					13540			
Element	ΔT_{eff}	$\Delta \log g$	$\Delta \xi$	$(\sum \sigma^2)^{1/2}$	ΔT_{eff}	$\Delta \log g$	$\Delta \xi$	$(\sum \sigma^2)^{1/2}$
	+200 K	+0.2	+0.4 km s ⁻¹		+200 K	+0.2	+0.3 km s ⁻¹	
Fe I	+0.13	0.00	-0.11	0.17	+0.15	-0.01	-0.13	0.20
Fe II	-0.17	+0.08	-0.11	0.22	-0.15	+0.10	-0.12	0.22
Na I	+0.13	0.00	-0.06	0.14	+0.14	-0.01	-0.07	0.16
Mg I	+0.13	-0.02	-0.16	0.21	—	—	—	—
Al I	—	—	—	—	+0.08	-0.01	-0.04	0.09
Si I	-0.04	+0.02	-0.04	0.06	+0.01	+0.02	-0.06	0.06
Ca I	+0.18	-0.02	-0.15	0.24	+0.18	-0.02	-0.16	0.24
Ti I	+0.25	0.00	-0.11	0.27	+0.23	-0.01	-0.11	0.26
Cr I	+0.25	-0.01	-0.20	0.32	+0.24	-0.01	-0.12	0.27
Ni I	+0.09	+0.02	-0.12	0.15	+0.12	+0.01	-0.13	0.18

13964					26606			
Element	ΔT_{eff}	$\Delta \log g$	$\Delta \xi$	$(\sum \sigma^2)^{1/2}$	ΔT_{eff}	$\Delta \log g$	$\Delta \xi$	$(\sum \sigma^2)^{1/2}$
	+300 K	+0.4	+0.6 km s ⁻¹		+450 K	+0.5	+1.0 km s ⁻¹	
Fe I	+0.18	-0.03	-0.16	0.24	+0.34	-0.06	-0.35	0.49
Fe II	-0.35	+0.22	-0.10	0.43	-0.36	+0.23	-0.17	0.46
Na I	+0.26	-0.01	-0.09	0.28	—	—	—	—
Mg I	+0.07	-0.02	-0.12	0.14	+0.12	0.00	-0.16	0.20
Al I	+0.15	-0.01	-0.04	0.16	+0.32	-0.01	-0.16	0.36
Si I	—	—	—	—	+0.24	+0.09	-0.19	0.32
Ca I	+0.35	-0.01	-0.25	0.43	—	—	—	—
Ti I	+0.50	-0.01	-0.13	0.52	+0.68	0.00	-0.59	0.90
Cr I	+0.28	-0.01	-0.08	0.29	+0.36	0.00	-0.10	0.37
Ni I	+0.05	+0.06	-0.09	0.12	+0.13	+0.10	-0.33	0.37

27955					28064			
Element	ΔT_{eff}	$\Delta \log g$	$\Delta \xi$	$(\sum \sigma^2)^{1/2}$	ΔT_{eff}	$\Delta \log g$	$\Delta \xi$	$(\sum \sigma^2)^{1/2}$
	+250 K	+0.2	+0.4 km s ⁻¹		+150 K	+0.3	+0.4 km s ⁻¹	
Fe I	+0.14	0.00	-0.11	0.18	+0.14	+0.03	-0.13	0.19
Fe II	-0.18	+0.10	-0.08	0.22	-0.11	+0.16	-0.07	0.21
Na I	—	—	—	—	+0.12	-0.01	-0.05	0.13
Mg I	+0.10	-0.02	-0.07	0.12	+0.05	0.00	-0.07	0.09
Al I	—	—	—	—	+0.08	-0.01	-0.04	0.09
Si I	+0.06	+0.03	-0.04	0.08	-0.05	+0.07	-0.09	0.12
Ca I	+0.22	-0.02	-0.12	0.25	+0.18	-0.01	-0.21	0.28
Ti I	+0.30	-0.01	-0.15	0.34	+0.23	-0.01	-0.09	0.25
Cr I	+0.24	-0.01	-0.10	0.26	+0.15	-0.01	-0.10	0.18
Ni I	+0.10	+0.02	-0.12	0.16	+0.10	+0.05	-0.18	0.21

31364					32782			
Element	ΔT_{eff}	$\Delta \log g$	$\Delta \xi$	$(\sum \sigma^2)^{1/2}$	ΔT_{eff}	$\Delta \log g$	$\Delta \xi$	$(\sum \sigma^2)^{1/2}$
	+150 K	+0.2	+0.3 km s ⁻¹		+250 K	+0.3	+0.6 km s ⁻¹	
Fe I	+0.14	0.00	-0.12	0.18	+0.15	0.00	-0.14	0.21
Fe II	-0.12	+0.13	-0.13	0.22	-0.21	+0.13	-0.09	0.26
Na I	+0.11	-0.01	-0.03	0.11	+0.19	-0.01	-0.08	0.21
Mg I	+0.05	0.00	-0.05	0.07	+0.04	-0.06	-0.10	0.12
Al I	—	—	—	—	+0.11	-0.01	-0.06	0.13
Si I	+0.01	+0.03	-0.04	0.05	—	—	—	—
Ca I	+0.16	-0.01	-0.17	0.23	—	—	—	—
Ti I	+0.22	-0.01	-0.09	0.24	+0.34	0.00	-0.11	0.36
Cr I	+0.25	-0.02	-0.17	0.30	+0.36	0.00	-0.10	0.37
Ni I	+0.14	+0.02	-0.12	0.19	+0.11	+0.04	-0.15	0.19

Notes. Each column gives the variation of the abundance caused by the variation in T_{eff} , $\log g$ and ξ . The last column for each star gives the compounded rms uncertainty of the second to fourth columns.

Table 6: Observed Fe I and Fe II lines.

Element	λ (Å)	χ (eV)	$\log gf$	Equivalent Widths (mÅ)							
				Star							
				11029	13540	13964	26606	27955	28064	31364	32782
Fe I	5162.27	4.18	0.079	—	153	—	—	—	—	143	—
	5198.71	2.22	-2.140	—	—	—	—	—	—	126	—
	5242.49	3.63	-0.970	—	—	—	—	—	126	98	—
	5288.52	3.69	-1.510	—	—	—	—	—	—	82	—
	5307.36	1.61	-2.970	160	140	—	—	149	—	—	—
	5315.05	4.37	-1.400	64	63	—	—	—	—	—	—
	5321.11	4.43	-1.190	—	—	—	—	—	69	—	—
	5322.04	2.28	-2.840	—	—	128	127	108	—	—	—
	5364.87	4.45	0.230	—	153	—	—	—	—	—	—
	5373.71	4.47	-0.710	95	97	84	—	—	—	84	—
	5389.48	4.42	-0.250	159	—	—	—	131	—	—	—
	5393.17	3.24	-0.720	—	156	—	—	—	—	149	—
	5417.03	4.42	-1.530	—	—	—	—	—	—	—	53
	5441.34	4.31	-1.580	45	—	—	—	—	42	—	—
	5445.04	4.39	-0.041	—	133	—	—	—	153	—	—
	5522.45	4.21	-1.400	70	—	—	39	—	—	—	—
	5531.98	4.91	-1.460	—	—	—	59	20	30	—	—
	5532.75	3.57	-2.000	—	—	40	—	—	—	—	—
	5554.90	4.55	-0.380	—	—	—	—	125	—	—	—
	5560.21	4.43	-1.040	85	—	—	67	—	—	70	—
	5567.39	2.61	-2.560	102	—	—	—	—	124	83	—
	5584.77	3.57	-2.170	—	—	—	—	—	—	68	—
	5624.02	4.39	-1.330	78	—	—	—	—	—	—	—
	5633.95	4.99	-0.120	—	—	105	107	76	—	—	—
	5635.82	4.26	-1.740	56	—	—	—	25	—	—	40
	5638.26	4.22	-0.720	116	—	—	—	—	—	—	131
	5686.53	4.55	-0.450	122	—	—	—	—	—	—	—
	5691.50	4.30	-1.370	—	—	—	—	64	83	—	—
	5705.47	4.30	-1.360	—	—	82	—	49	67	51	76
	5717.83	4.28	-0.979	—	—	—	88	80	—	—	—
	5731.76	4.26	-1.150	101	—	—	—	—	91	—	—
	5806.73	4.61	-0.900	75	—	—	—	—	—	—	80
	5814.81	4.28	-1.820	—	—	—	—	—	37	29	—
	5852.22	4.55	-1.180	78	76	—	—	—	—	51	—
	5883.82	3.96	-1.210	—	—	95	—	79	101	—	—
	5916.25	2.45	-2.990	—	99	97	—	—	108	86	99
	5934.65	3.93	-1.020	111	103	105	—	113	—	—	—
	6020.17	4.61	-0.210	—	—	—	—	128	—	—	—
	6024.06	4.55	-0.060	141	—	124	—	128	123	—	—
	6027.05	4.08	-1.090	—	107	112	92	87	—	—	—
	6056.01	4.73	-0.400	—	—	92	—	99	—	80	127
	6079.01	4.65	-0.970	76	—	60	—	—	—	—	—
	6082.71	2.22	-3.580	—	—	—	—	—	98	—	—
	6093.64	4.61	-1.350	46	—	—	—	—	—	—	—
	6096.66	3.98	-1.780	70	65	—	—	—	—	65	—
	6120.25	0.91	-5.950	—	—	—	—	—	42	—	—
	6151.62	2.18	-3.290	98	92	112	—	79	103	—	—
	6157.73	4.08	-1.110	—	—	—	85	—	—	85	—
	6165.36	4.14	-1.470	64	66	75	93	78	—	71	—
	6170.51	4.79	-0.380	—	102	—	—	—	—	—	—
	6173.34	2.22	-2.880	126	—	—	—	—	146	—	155
	6187.99	3.94	-1.570	82	77	89	—	57	88	72	—
	6200.31	2.60	-2.440	130	—	133	—	118	144	—	—

Table 6, continued

Element	λ (Å)	χ (eV)	$\log gf$	Equivalent Widths (mÅ)								
				Star								
				11029	13540	13964	26606	27955	28064	31364	32782	
Fe I	6213.43	2.22	-2.480	149	—	—	—	—	—	—	—	—
	6254.26	2.28	-2.440	157	—	—	—	—	—	—	—	—
	6265.13	2.18	-2.550	147	—	—	—	143	—	124	—	—
	6322.69	2.59	-2.430	137	—	—	—	124	—	—	—	142
	6380.74	4.19	-1.320	86	84	—	—	83	81	—	—	—
	6392.54	2.28	-4.030	62	—	—	—	35	51	—	—	—
	6411.65	3.65	-0.660	—	139	—	—	—	—	—	—	—
	6421.35	2.28	-2.010	—	—	—	—	149	—	151	—	—
	6436.41	4.19	-2.460	—	—	—	—	20	10	—	—	—
	6469.19	4.83	-0.620	98	79	—	116	75	72	—	—	—
	6574.23	0.99	-5.020	—	86	—	101	61	102	78	—	—
	6591.31	4.59	-2.070	20	—	—	—	—	—	—	—	—
	6593.87	2.44	-2.420	—	—	—	—	129	—	—	—	—
	6597.56	4.79	-0.920	60	—	—	80	—	—	46	—	—
	6608.03	2.28	-4.030	61	37	58	90	—	63	—	—	—
	6609.11	2.56	-2.690	122	—	—	—	—	110	—	—	133
	6646.93	2.61	-3.990	—	23	—	—	18	25	—	—	—
	6653.85	4.14	-2.520	—	—	—	—	—	—	22	—	—
	6703.57	2.76	-3.160	68	79	78	53	41	—	—	—	55
	6710.32	1.80	-4.880	—	—	—	68	—	—	—	—	—
	6739.52	1.56	-4.950	39	—	57	86	—	58	34	—	59
	6750.15	2.42	-2.620	118	—	—	147	—	—	118	—	148
	6752.71	4.64	-1.200	59	47	—	—	45	—	60	—	—
	6806.85	2.73	-3.210	77	—	97	113	—	83	—	—	—
	6820.37	4.64	-1.170	—	74	—	—	—	43	50	—	—
	6841.34	4.61	-0.600	124	—	—	—	—	—	—	—	—
	6851.64	1.61	-5.320	—	—	—	52	—	—	24	—	—
6858.15	4.61	-0.930	—	91	75	—	88	81	—	—	64	
7130.92	4.22	-0.700	129	126	126	—	111	115	113	—	—	
7132.99	4.08	-1.610	—	—	76	—	—	—	66	—	—	
Fe II	5132.66	2.81	-4.000	—	—	—	—	26	—	—	—	—
	5234.62	3.22	-2.240	—	—	—	—	108	—	—	—	—
	5425.25	3.20	-3.210	60	70	74	39	44	—	75	—	59
	5534.83	3.25	-2.770	95	—	—	—	76	—	—	—	—
	5991.37	3.15	-3.560	66	—	—	—	—	—	—	—	—
	6084.10	3.20	-3.800	39	—	—	—	17	26	—	—	—
	6149.25	3.89	-2.720	53	—	49	45	—	42	70	—	—
	6247.55	3.89	-2.340	82	86	56	—	—	78	81	—	—
	6369.46	2.89	-4.110	—	—	—	—	—	43	—	—	—
	6416.92	3.89	-2.680	63	67	—	—	43	41	—	—	—
	6432.68	2.89	-3.580	61	—	—	36	—	—	—	—	—

Table 7: Other lines studied.

Element	λ	χ (eV)	$\log gf$	Ref	Equivalent Widths (mÅ)							
					Star							
					11029	13540	13964	26606	27955	28064	31364	32782
Na I	6154.22	2.10	-1.51	PS	73	79	—	—	—	66	59	88
Na I	6160.75	2.10	-1.21	R03	—	99	89	—	—	—	—	—
Mg I	4730.04	4.34	-2.39	R03	81	—	—	—	—	—	—	—
Mg I	5711.10	4.34	-1.75	R99	146	—	—	—	127	—	—	—
Mg I	7387.70	5.75	-0.87	MR94	—	—	115	120	77	—	54	—
Mg I	8717.83	5.91	-0.97	WSM	—	—	—	88	—	70	—	129
Mg I	8736.04	5.94	-0.34	WSM	—	—	—	—	—	112	91	—
Al I	6698.67	3.14	-1.63	R03	—	—	—	74	—	—	—	—
Al I	7835.32	4.04	-0.58	R03	—	62	45	—	—	32	—	82
Al I	7836.13	4.02	-0.40	R03	—	72	59	—	—	54	—	—
Al I	8772.88	4.02	-0.25	R03	—	—	—	—	—	66	—	—
Al I	8773.91	4.02	-0.07	R03	—	—	—	—	—	65	—	—
Si I	5793.08	4.93	-2.06	R03	—	76	—	—	51	—	—	—
Si I	6125.03	5.61	-1.54	E93	55	56	—	—	—	—	40	—
Si I	6131.58	5.62	-1.69	E93	—	—	—	—	—	—	45	—
Si I	6145.02	5.61	-1.43	E93	58	—	—	—	—	—	—	—
Si I	6155.14	5.62	-0.77	E93	—	95	—	—	86	—	79	—
Si I	8728.01	6.18	-0.36	E93	—	—	—	97	—	—	—	—
Si I	8742.45	5.87	-0.51	E93	—	—	—	—	—	86	—	—
Ca I	6161.30	2.52	-1.27	E93	—	107	125	—	—	—	—	—
Ca I	6166.44	2.52	-1.14	R03	87	112	140	—	101	—	89	—
Ca I	6169.04	2.52	-0.80	R03	129	—	154	—	—	—	—	—
Ca I	6169.56	2.53	-0.48	DS91	142	—	—	—	—	—	—	—
Ca I	6455.60	2.51	-1.29	R03	78	—	121	—	64	—	—	—
Ca I	6471.66	2.51	-0.69	S86	—	132	—	—	115	117	106	—
Ti I	4758.12	2.25	0.420	MFK	—	92	—	125	—	—	—	—
Ti I	5039.96	0.02	-1.130	MFK	—	—	—	—	148	—	—	—
Ti I	5043.59	0.84	-1.733	MFK	63	—	—	—	—	—	—	—
Ti I	5062.10	2.16	-0.464	MFK	—	—	—	—	50	—	—	—
Ti I	5113.45	1.44	-0.880	E93	—	—	—	—	—	93	—	—
Ti I	5223.63	2.09	-0.559	MFK	—	—	50	—	—	—	—	—
Ti I	5295.78	1.05	-1.633	MFK	—	—	—	—	—	72	—	—
Ti I	5490.16	1.46	-0.937	MFK	—	69	—	—	—	—	—	—
Ti I	5689.48	2.30	-0.469	MFK	—	—	—	—	—	46	—	64
Ti I	5866.46	1.07	-0.871	E93	106	—	—	—	109	—	95	—
Ti I	5922.12	1.05	-1.465	MFK	—	—	83	—	—	—	76	—
Ti I	5978.55	1.87	-0.496	MFK	81	75	—	—	75	—	—	—
Ti I	6091.18	2.27	-0.370	R03	67	—	—	—	—	—	42	—
Ti I	6126.22	1.07	-1.370	R03	84	—	103	128	—	81	—	101
Ti I	6258.11	1.44	-0.355	MFK	—	—	118	—	—	—	—	—
Ti I	6261.11	1.43	-0.480	B86	—	—	127	—	105	—	—	—
Ti I	6554.24	1.44	-1.219	MFK	—	—	49	—	—	—	—	100
Cr I	5193.50	3.42	-0.720	MFK	27	—	—	—	—	—	—	—
Cr I	5214.13	3.37	-0.740	MFK	—	—	—	—	20	—	—	—
Cr I	5296.70	0.98	-1.390	GS	154	—	—	—	—	—	—	—
Cr I	5304.18	3.46	-0.692	MFK	—	—	—	42	—	—	—	—
Cr I	5345.81	1.00	-0.980	MFK	—	—	—	—	—	—	151	—
Cr I	5348.32	1.00	-1.290	GS	158	132	—	—	144	—	—	—
Cr I	5783.07	3.32	-0.500	MFK	—	—	64	—	47	73	—	—
Cr I	5787.93	3.32	-0.080	GS	—	58	—	—	—	75	—	—
Cr I	6330.09	0.94	-2.920	R03	—	57	—	—	—	—	65	85
Ni I	4904.42	3.54	-0.170	MFK	—	125	—	—	143	—	—	136
Ni I	4935.83	3.94	-0.360	MFK	—	83	—	—	88	70	—	—

Table 7, continued.

Element	λ	$\chi(\text{eV})$	$\log gf$	Ref	Equivalent Widths (mÅ)							
					Star							
					11029	13540	13964	26606	27955	28064	31364	32782
Ni I	4953.21	3.74	-0.660	MFK	—	—	—	—	88	—	—	—
Ni I	5010.94	3.63	-0.870	MFK	—	—	87	—	—	—	—	—
Ni I	5578.73	1.68	-2.640	MFK	108	—	—	—	—	110	90	—
Ni I	5593.75	3.90	-0.840	MFK	60	—	—	—	73	45	—	85
Ni I	5643.09	4.17	-1.250	MFK	24	40	—	—	—	—	—	—
Ni I	5748.36	1.68	-3.260	MFK	—	—	—	—	—	—	—	73
Ni I	5805.23	4.17	-0.640	MFK	—	—	—	—	72	43	—	—
Ni I	6053.69	4.24	-1.070	MFK	—	49	—	—	—	—	—	—
Ni I	6086.29	4.27	-0.510	MFK	62	81	—	—	—	50	—	—
Ni I	6128.98	1.68	-3.320	MFK	—	78	—	—	64	67	57	—
Ni I	6176.82	4.09	-0.264	R03	—	—	—	—	93	—	—	—
Ni I	6186.72	4.11	-0.960	MFK	56	—	47	—	—	—	50	—
Ni I	6204.61	4.09	-1.150	MFK	42	—	—	—	—	—	—	—
Ni I	6223.99	4.11	-0.980	MFK	—	—	57	—	—	—	—	—
Ni I	6230.10	4.11	-1.260	MFK	—	—	44	—	—	—	33	—
Ni I	6327.60	1.68	-3.150	MFK	—	—	—	—	85	—	63	—
Ni I	6482.81	1.94	-2.630	MFK	—	—	—	—	83	—	—	100
Ni I	6532.88	1.94	-3.390	MFK	—	—	—	—	57	44	—	—
Ni I	6586.32	1.95	-2.810	MFK	—	84	—	—	—	—	—	95
Ni I	6635.14	4.42	-0.830	MFK	—	41	—	—	—	—	40	—
Ni I	6643.64	1.68	-2.030	MFK	153	144	—	—	—	—	129	—
Ni I	6767.78	1.83	-2.170	MFK	141	—	—	—	—	—	105	—
Ni I	6772.32	3.66	-0.970	R03	73	—	—	83	—	84	—	—
Ni I	7788.93	1.95	-1.990	E93	151	140	—	—	—	—	130	—

References: B86: Blackwell et al. (1986); Ca07: Carretta et al. (2007); D2002: Depagne et al. (2002); DS91: Drake & Smith (1991); E93: Edvardsson et al. (1993); GS: Gratton & Sneden (1988); MFK: Martin et al. (2002); MR94: McWilliam and Rich (1994); PS: Preston & Sneden (2001); R03: Reddy et al. (2003); R99: Reddy et al. (1999); WSM: Wiese et al. (1969).

Table 8: Adopted solar abundances.

Element	This work	Grevesse & Sauval (1998)	Asplund <i>et al.</i> (2009)
Fe	7.50	7.50	7.50
Na	6.26	6.33	6.24
Mg	7.55	7.58	7.60
Al	6.31	6.47	6.45
Si	7.61	7.55	7.51
Ca	6.37	6.36	6.34
Ti	4.93	5.02	4.95
Cr	5.65	5.67	5.64
Ni	6.29	6.25	6.22

solutions, symmetric with respect to A0 spectral type. We therefore analysed the results of the three aforementioned stars in more detail. We indeed found a secondary solution for the star #8542, with a local minimum of the χ^2 statistics, on the other side of the Balmer minimum at 10100 K. However, this minimum of χ^2 is shallower than the main solution at 8100 K, which is therefore more likely and should be preferred. We did not find such a secondary minimum for star #12018, and the fitting routine converged to the same solution at 8700 K even if it was forced to start from a hot first guess at $T_{\text{Jeff}} > 12000$ K. On the other hand, a cooler solution for the star #6507 is not acceptable, because $T_{\text{eff}} < 9000$ K would return $E(V - I) < 0.37$ and a distance $d \approx 10$ kpc, clearly offset from the reddening-distance relation depicted by the other stars in box C and D (see below in Fig. 10). In addition, this object is of little interest because most likely not a genuine MS star (see later). In conclusion, our tests indicate that, despite fitting one Balmer line only, the solutions we find for these three stars are either the only one acceptable, or the most likely. To check the effects of the use of solar metallicity models, we repeated the measurements with models with $[\text{Fe}/\text{H}] = -0.5$, but we found that the results changed by less than 0.5σ in all the cases. The results are given in Table 10. The resulting surface gravities indicate that all the targets are MS stars, with the exception of the star #6507. The measurements for this star are affected by large errors, so that it could still be considered a MS object within the error bars, but the high $\log g$ value suggests that this could be a foreground sub-dwarf B-type (sdB) star.

The temperature of Box D targets was determined by fitting the profile of temperature-sensitive lines with synthetic spectra drawn from the library of Coelho et al. (2005). We adopted the same routines of Moni Bidin et al. (2010), where detailed information about the measurement procedure can be found. The main feature for our measurements was the H_α Balmer line, which is a good indicator of temperature in the range $T_{\text{eff}} = 5000\text{--}6500$ K, insensitive to metallicity and surface gravity (Fuhrmann et al. 1994). Its wings were fitted with solar-metallicity templates in steps of 250 K, and the χ^2 was minimised to find the best estimate of the target temperature. We verified that varying the metallicity of the synthetic templates had only negligible effects on the results.

One gravity-sensitive feature was observable in the spectrum of some targets, either the MgIb triplet (Kuijken & Gilmore 1989) or the Na I doublet at 5890–5893 Å. However, the low resolution of the data prevented an estimate of $\log g$, because only large mismatches (> 1 dex) between the template and object line wings could be appreciated. Hence, the targets were assumed MS stars along the whole process, with a fixed surface gravity of $\log g = 4.1$ dex, as strongly suggested by their position in the CMD. We nevertheless confirmed this hypothesis by checking that the profiles of available lines were compatible with it. On the other hand, this assumption was also confirmed by later distance estimates because, had one of these stars been either a faint sub-dwarf or a bright giant, its distance would have resulted extremely large or short, respectively, which is not the case (see Table 10). The MgIb triplet and the Na I doublet were instead used to derive independent estimates of T_{eff} , with a procedure identical to that used for H_α . The final results and their associated errors were obtained from the average and the error-of-the-mean of these measurements.

4.4. Reddening and distances

The reddening for the stars of box B were estimate using isochrones of Bertelli et al. (2008, 2009) to obtain the $(V - I)$ intrinsic color of each star. In the Table 3 we show $E(V - I)$ values obtained for the stars of box B. We also calculated the distances for each star of the box B using the equation:

$$\begin{aligned} \log d \text{ (pc)} &= 1/2[\log \frac{M_{\star}}{M_{\odot}} + 0.4(V - A_V + BC) \\ &+ 4 \log T_{\text{eff}} - \log g_{\star} - 10.62]. \end{aligned} \quad (4)$$

Where T_{eff} and $\log g_{\star}$ are the effective temperature and surface gravity, respectively, and M is the mass obtained through the evolutionary tracks of Bertelli et al. (2008) and Bertelli et al. (2009). The photometric data of Table 2 were combined with bolometric corrections (BC) defined by the relations of Alonso et al. (1999). The extinction in V (A_V) for each star was calculated using the reddening $E(V - I)$ shown in the Table 3, the non-standard absorption law valid for the third Galactic quadrant, where $R_V=2.9$ (Turner et al. 2014) and $E(B - V) = 0.7955 \times E(V - I)$ (Turner et al. 2011). For the Sun we adopted $M_{\text{bol}\odot} = 4.74$ mag (Bessell et al. 1998), $T_{\text{eff}\odot} = 5700$ K and $\log g_{\odot} = 4.3$ dex.

We also performed a rough estimate of the age of the stars from box B using spectroscopic atmospheric parameters and isochrones of Bertelli et al. (2008) and Bertelli et al. (2009). We note that such a sample is composed of a great mix of stars with the age ranging from 1.2 Myr to 10 Gyr. This huge range is not unexpected when considering a sample containing both thin and thick disk stars.

The reddening and distance of box C and D stars were derived similarly. The intrinsic colours and absolute magnitudes of box C stars were derived from comparison of their position in the temperature–gravity plane with the same solar-metallicity isochrones used for box B. The intrinsic color, compared with the observed one, returned the reddening $E(V - I)$, which was used to derive A_V with the same equations given above. As we had no gravity information for box D stars, but we argued that they are all MS objects, we adopted for them the absolute magnitude of solar-metallicity ZAMS objects at the corresponding temperature. From the derived absolute magnitude, the observed V magnitude, and A_V , the distances were straightforwardly computed. We chose to use $(V - I)$ as temperature indicator for consistency with what done in Box B. However, a bluer color could be a better choice for Box C, where the stars are noticeably hotter than in the other two groups. To test if our choice would alter the results, we repeated the procedure using $(B - V)$ instead of $(V - I)$ in Box C. The reddening values thus derived are compatible within errors with those previously obtained, with a mean difference and standard deviation of -0.04 ± 0.05 mag, and no clear trend with temperature.

Table 9: Atmospheric parameters from spectroscopy of box C.

ID	T_{eff} K	$\log g$ dex	$v \sin i$ km s ⁻¹	$\langle \text{RV} \rangle$ km s ⁻¹	$E(V - I)$	$(V - Mv)_0$	d (pc)
6507*	14500±3200	5.5±1.0	20	112±3	0.68±0.05	15.68±0.79	14400±5200
8542*	8100±4200	4.8±3.2	120	99±45	0.38±0.28	14.01±1.74	6400±5100
9227	9800±1800	4.2±0.8	210	75±13	0.47±0.20	14.21±0.78	7100±2800
12018*	8700±800	4.2±0	0*	97±6	0.41±0.09	13.52±0.39	5100±900
13279	13100±1100	4.4±0.3	10	63±5	0.78±0.03	14.63±0.30	9000±1200
16940	10800±2400	4.1±0.3	310	69±11	0.71±0.06	14.45±0.75	8200±2800
24772	12000±1400	4.4±0.5	60	88±2	0.56±0.05	14.71±0.41	9100±1700
28816	9700±900	3.6±0.5	70	96±2	0.50±0.08	13.87±0.38	6100±1000
30971	11400±800	4.6±0.3	90	78±9	0.77±0.03	14.33±0.25	7800±900
31183	14000±1600	4.4±0.5	40	62±2	0.82±0.03	15.22±0.41	11900±2200
32089	12200±700	4.3±0.3	230	84±1	0.75±0.03	13.98±0.22	6600±900

Notes. *: no H_β line.

Table 10: Atmospheric parameters from spectroscopy of box D.

ID	T_{eff} (K)	$\langle \text{RV} \rangle$ (km s ⁻¹)	$E(V - I)$	$(V - Mv)_0$	d (pc)
7421	5850±40	76±8	0.35±0.03	13.78±0.09	5700±200
9011	6240±180	101±12	0.38±0.05	13.63±0.29	5300±700
9834	6210±150	74±3	0.43±0.04	14.20±0.24	6900±800
11923	—	106±8	—	—	—
19341	5990±200	88±13	0.38±0.05	13.94±0.34	6100±1000
22319	5885±20	125±6	0.31±0.02	13.43±0.05	4860±100
23667	6330±50	139±7	0.38±0.03	13.57±0.10	5200±200
31274	5910±125	135±2	0.37±0.04	13.84±0.22	5900±600
36132	—	91±2	—	—	—

5. Results of abundance analysis

The chemical abundance is one of the main pillars in characterising stellar populations, and the spectral analysis is the most reliable technique for obtaining of the star’s chemistry. The chemical pattern in the stars allows one, for example, to distinguish which are the stars from the thick and from thin disk (e.g., Masseron & Gilmore 2015), or even if a cluster (or star) has extragalactic origin (e.g., Sbordone et al. 2015). In this Section we present the results of our chemical analysis for the red clump stars in order to characterise this stellar population.

5.1. Metallicity and iron-peak elements

Red clump stars have been widely used to characterise the structure of the Galaxy (e.g., Lee et al. 2015; Romero-Gómez et al. 2015) mainly because they are bright enough and numerous (Bienaymé et al. 2014; Wan et al. 2015). In Galactic clusters, such stars are characterised by having a similar chemical abundance, unlike the field red clump stars, which present a larger dispersion.

In Table 3, we show the metallicity derived for eight red clump stars from box B. We found that our sample of field red clump stars covers the metallicity range of $-0.68 \leq [\text{Fe}/\text{H}] \leq 0.03$. Despite the wide dispersion in metallicity of our red clump stars, some of them have similar characteristics. Two of the targets stars with the lowest metallicity (stars #13964 and #28064) present high estimate for the distances (20 and 12 kpc, respectively), although our results for the star #13964 are affected by a large uncertainty in atmospheric parameters and distance due to the low S/N of its spectrum (see Table 3). Despite its higher metallicity ($[\text{Fe}/\text{H}] = -0.24$), the target #31364 also exhibits a very high distance, $d \approx 23$ kpc. We also noted that these three very distant stars have slightly similar radial velocities (73.9, 68.0 and 65.6 km/s). For the stars #11029, #13540, #27955, and #32782, our results for the metallicity and distance indicate that they are located either near the closest edge of the outer disk or in the transition region between the outer and inner disk ($9 \leq R_{GC} \leq 13$ kpc), where a large scatter of metallicity is found (Magrini et al. 2009).

The Type Ia supernovae are the main sources of enrichment of the interstellar medium with Fe and iron-peak elements, like Cr and Ni. Therefore, the chemical study of iron-peak elements is important to analyse the type Ia supernovae production rate for the formation of the observed stellar population, being this rate, for example, a key parameter to set the Initial Mass Function (IMF). For our sample of the red clump stars, the ranges in abundance ratios of $[\text{X}/\text{Fe}]$ for Cr and Ni are $-0.09 \leq [\text{Cr}/\text{Fe}] \leq +0.35$ and $-0.22 \leq [\text{Ni}/\text{Fe}] \leq +0.24$. In Fig. 8 and 9 we show the abundance ratio of $[\text{X}/\text{Fe}]$ for our sample of red clump field star, for field dwarf from Bensby et al. (2014), for disk Cepheids from Lemasle et al. (2013) and Genovali et al. (2015), and also for open clusters, as described in the Figure caption.

The $[\text{Cr}/\text{Fe}]$ and $[\text{Ni}/\text{Fe}]$ ratios are close to solar for all our red clump targets, as observed among disk field dwarfs and open cluster from literature in the range $-1 \leq [\text{Fe}/\text{H}] \leq 0$ (see Fig. 8).

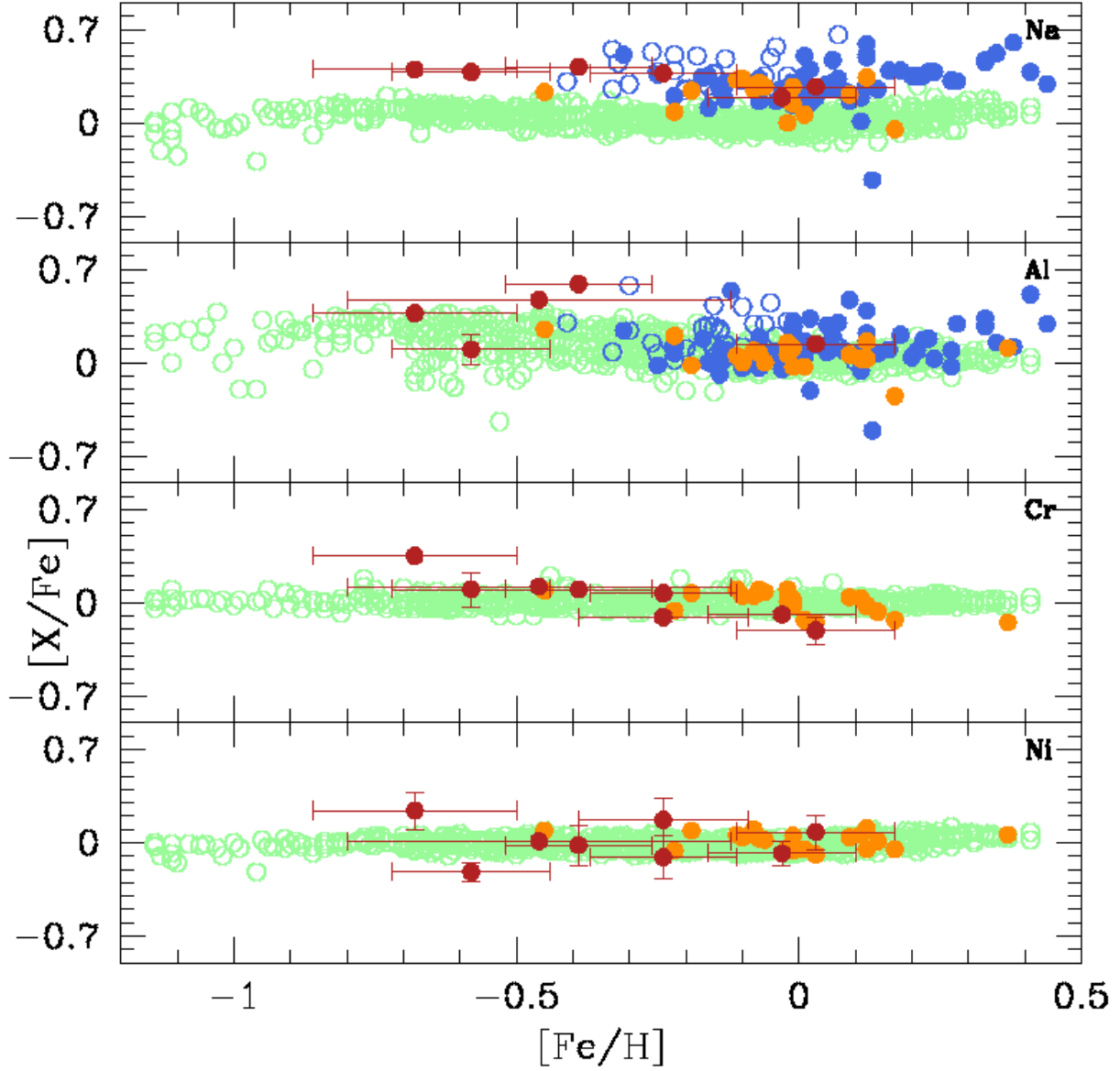


Fig. 8.— Abundance ratios $[\text{X}/\text{Fe}]$ vs. $[\text{Fe}/\text{H}]$. Light green open circles: field dwarf of Bensby et al. (2014); Blue open circles: Cepheids of disk of Lemasle et al. (2013); Blue filled circles: Cepheids of disk of Genovali et al. (2015); Red filled circles: our sample of red clump field stars; Orange filled circles: open clusters from literature (Tombaugh 1 of Sales Silva et al. (2016); NGC 6192, NGC 6404 and NGC 6583 of Magrini et al. (2010); NGC 3114 of Katime Santrich et al. (2013); NGC 2527, NGC 2682, NGC 2482, NGC 2539, NGC 2335, NGC 2251 and NGC 2266 of Reddy et al. (2013); NGC 4337 of Carraro et al. (2014); Trumpler 20 of Carraro et al. (2014); NGC 4815 and NGC 6705 of Magrini et al. (2014); Cr 110, Cr 261, NGC 2477, NGC 2506 and NGC 5822 of Mishenina et al. (2015).

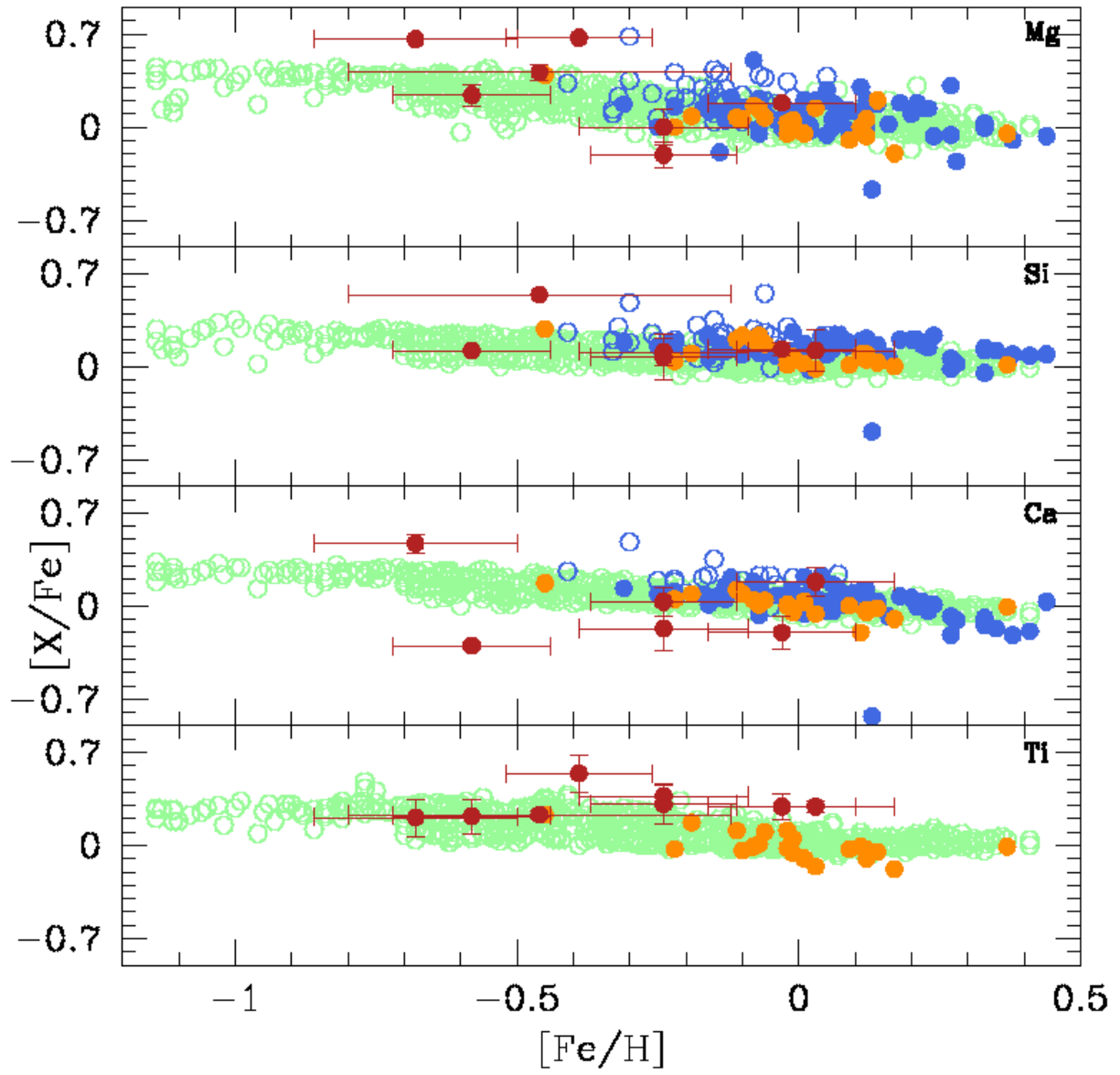


Fig. 9.— Abundance ratios $[\text{X}/\text{Fe}]$ vs. $[\text{Fe}/\text{H}]$. Symbols have the same meaning as in Fig. 8.

The abundance ratio of Nickel in the Milky Way, in particular, is locked to solar value at any metallicity (e.g., Sneden et al. 2004). This is usually assumed as evidence that Nickel is synthesised in the same astrophysical sites as iron, and in a constant proportion with respect to it. However, Sbordone et al. (2007) found that the Sagittarius dwarf spheroidal galaxy (Sgr dSph) is depleted in Nickel by ≈ 0.3 dex in the whole range $-1 \leq [\text{Fe}/\text{H}] \leq 0$, a behaviour that could extend even down to $[\text{Fe}/\text{H}] = -2$ (Sbordone et al. 2015). This exotic chemical composition was, however, not observed among metal-poor ($[\text{Fe}/\text{H}] \leq -2$) globular clusters in Fornax (Letarte et al. 2006), so it is not clear if a lower $[\text{Ni}/\text{Fe}]$ should be expected for all dwarf galaxies at any metallicity. In any case, we find no evidence of an exotic, potentially extragalactic abundance of Nickel in our sample.

5.2. Na, Al and α -elements

Chemical abundances of the α -elements are constantly used to reveal the history of star formation and define the structure of the galactic disk. In the disk, stars with high abundance of α -elements are associated with the thick disk while stars with solar ratios are usually classified as belonging to the thin disk (e.g., Bensby et al. 2005). The separation of the disk into two components is usually interpreted as evidence that the stars of thick disk had a rapid star formation with Type-II supernovae contributing more to the chemical enrichment of the interstellar medium than in the thin disk. In Table 4 we present the abundance ratios for the alpha elements Mg, Si, Ca and Ti for the eight field red clump stars. We noted that the $[\text{X}/\text{Fe}]$ ratios for Ti and Si are super-solar for our sample of red clump star. For Mg, the $[\text{X}/\text{Fe}]$ ratios shows sub-solar or solar values for two stars (#27955 and #31364) while for the other red clump star we got super-solar values. And finally, the $[\text{Ca}/\text{Fe}]$ ratio shows super-solar values for three red clump stars and sub-solar for another three stars (#11029, #27955, and #2806, with values -0.20 , -0.17 and -0.30 , respectively).

On average, the stars #13540, #13964, #26606, and #32782 have a high α -element abundances, with values of $[\alpha/\text{Fe}]$ ratios of 0.20 ± 0.09 , 0.45 ± 0.23 , 0.39 ± 0.16 and 0.60 ± 0.09 , respectively. Then, this stars are probably members of the thick disk. The other red clump stars in our sample (ID 1102, 27955, 28064 and 31364) present $[\alpha/\text{Fe}]$ between 0.05 and 0.10 dex, and therefore probably belong to the galactic thin disk population.

Yong et al. (2005), Carney et al. (2005), and Yong et al. (2006) found that field and cluster stars in the outer galactic disk show enhancements for the alpha-elements, $[\alpha/\text{Fe}] \sim 0.2$, and a metallicity of approximately ~ -0.5 dex. However, in a more recent study of giant stars in the field of outer disk, Bensby et al. (2011) detected thin disk of stars with $[\alpha/\text{Fe}] \sim 0.0$ and a lack of stars with chemical pattern of the thick disk ($[\alpha/\text{Fe}] \geq 0.2$), even for stars far above the Galactic plane. Bensby et al. (2011) concluded that this lack of thick disk stars was apparent, and was caused by the scale-length of the thick disk be significantly shorter than that of the thin disk. Our rough estimate of the distance for the red clump stars of the box B situate many of these stars in the outer disk ($R_{GC} \gtrsim 13$ kpc). The two disk populations (thin and thick) were detected in our sample of stars of the outer disk. For the nearest red clump stars ($1.2 \leq d \leq 5.3$ kpc), we detected three stars

with thick disk properties (stars 1#3540, #26606 and #32782) and two belonging to the thin disk (stars #11029 and #27955). The second most distant star in our sample (star #13964 with $d \sim 20$ kpc) is also the star with lower metallicity ($[\text{Fe}/\text{H}] = -0.68$) and that has an average abundance of alpha elements of $[\alpha/\text{Fe}] = 0.45 \pm 0.23$. This star by its chemical pattern can be classified as a star of the thick disk or of the Galactic disk-halo transition region. The region of Galactic disk-halo transition is characterised by stars with $-1.20 \leq [\text{Fe}/\text{H}] \leq 0.55$, and α -poor and α -rich stars (Hawkins et al. 2015). Our estimate for the distance of the star #13964 ($d \sim 21$ kpc), despite its significant uncertainty, may also indicate that this star is outside the Galaxy. In this case, the star 13964 may have been lost by the Milky Way or belongs to an extragalactic object in the vicinity of the Milky Way. The other two stars situated on the edge of outer disk (stars #28064 and #31364) have a chemical pattern typical of thin disk ($[\alpha/\text{Fe}] \sim 0.0$). So our sample, although small, shows that the thin disk is probably dominant in the most extreme regions of the disk, in accordance with the conclusions of Bensby et al. (2011). Study of stars located in the extreme outer regions of the disk can quantify how warped and flared is the galactic disk, as well as, how the stellar populations in these regions evolve. Furthermore, the interesting finding of a significant amount of stars at the end of galactic disk with large estimates of distance from the galactic plane (like the stars #13964, #28064, and #31364) can also reveal a significant mixing between stars from the disk and the halo caused by the warped and flared disk. But what this interaction between the warped and flared disk and the halo implies for the evolution of stellar populations in this extreme region of the Galaxy? In this region, do we have a stellar population predominantly α -rich or α -low? And what is the metallicity range? A major difficulty for a reliable study of the structure of extreme outer region of the disk is an estimated distance that often comes with large uncertainties (as our estimate for the star 13964). Incoming data from Gaia mission will surely enable more solid distance estimates for many stars and put us in a better position to answer to these questions.

The production of the Na in the stellar interior is performed during the hydrostatic carbon burning in massive stars (Woosley & Weaver 1995), and also is affected by NeNa cycle in the H-burning envelope in intermediate-mass and massive stars (Denisenkov & Denisenkova 1990). In giant stars, the chemical abundance of Na is important to investigate the mixing processes occurring in the stellar interior, like the first dredge-up, *thermohaline* instability, and rotation-induced mixing (Charbonnel & Lagarde 2010).

The effects of the non-local thermodynamic equilibrium (NLTE) are considerable in the abundance of Na (Gratton et al. 1999; Lind et al. 2011) and should be taken into account. In our analysis, we used the corrections of Gratton et al. (1999) to estimate such effects. Table 4 show the $[\text{Na}/\text{Fe}]$ ratios for six red clump stars. The abundance ratio $[\text{Na}/\text{Fe}]$ for our field red clump stars presents an overabundance that goes from 0.19 to 0.42. In Fig. 5 we see that the $[\text{Na}/\text{Fe}]$ ratio for our sample are overabundant when compared to disk dwarfs from Bensby et al. (2014). The overabundance of $[\text{Na}/\text{Fe}]$ ratio in giant stars with respect dwarf stars indicates the importance of the chemical mixing phenomena occurring in the stellar interior during the giant phase (Pasquini et al. 2004).

Al is mainly produced during the hydrostatic carbon and neon burning in massive stars (Woosley & Weaver 1995), and can be affected by MgAl cycle in H-burning layers at high temperatures (Arnould & Mowlavi 1995). We observed an overabundance of Al with respect to Fe for our red clump sample, with a range of $0.10 \leq [\text{Al}/\text{Fe}] \leq 0.59$ (see Table 4). The stars that present the highest values for the $[\text{Al}/\text{Fe}]$ ratio (#13964, #26606, and #32782) are also the stars that have a high overabundance of α -elements.

While α -elements are overabundant in stellar populations characterised by a fast star formation history such as the Galactic thick disk, the stars in dwarf galaxies are usually α -depleted. This is because the slow star formation rate in these low-density environments prevents the yields of Type-II supernovae from dominating the pollution of the interstellar medium. In fact, the average α -elements abundance of Sgr dSph stars in the range $-1 \leq [\text{Fe}/\text{H}] \leq 0$ is $[\alpha/\text{Fe}] \approx -0.2$ (Sbordone et al. 2007). Similar sub-solar α -abundances were found by Sbordone et al. (2005) in three field stars, and they were the basis of their claim of an extragalactic origin for their targets. Na and Al also are depleted in intermediate-metallicity Sgr dSph stars by ≈ -0.3 and -0.5 dex, likely because the astrophysical sites of their synthesis, massive and intermediate-mass stars, is the same where most of the α -elements are produced. In this context, we note that none of our box B stars show abundances that differ from the Galactic trend. The α -elements, Na, and Al abundances, along with Ni that we discussed in the previous Section, are either close to solar, or super-solar for the most metal-poor targets, in full agreement with the general trend of Galactic thin and thick disk stars. We therefore conclude that there is no evidence of an extragalactic origin for any of the studied object.

In the discussion section we put the red clump stars together with the other stars of our sample in the context of the structure of the third Galactic quadrant and try to make connections between the different populations so far analysed .

6. Discussion and conclusions

In the following we are going to discuss the results of our photometric and spectroscopic analysis and attempt to draw a coherent scenario out of them.

The targets in box D (see Fig. 1) belong to a thick, faint MS in the background of the cluster Tombaugh 1. The observed objects (see Table 10) are all F8-G2 spectral type stars with similar reddening, spanning a narrow range in distance (5–7 kpc, 5.7 kpc on average). They trace a tight sequence in the CMD. MS stars with these spectral types must be younger than ≈ 9 Gyr, and the MS in the CMD continues blue-ward to even higher temperatures (group in box C, see below). Hence, this MS traces an intermediate-age stellar population, and it cannot be associated to the Galactic halo or thick disk. The distance spread is most likely physical and not only a product of measurement errors, because the stars follow a clear reddening-distance relation, as shown in

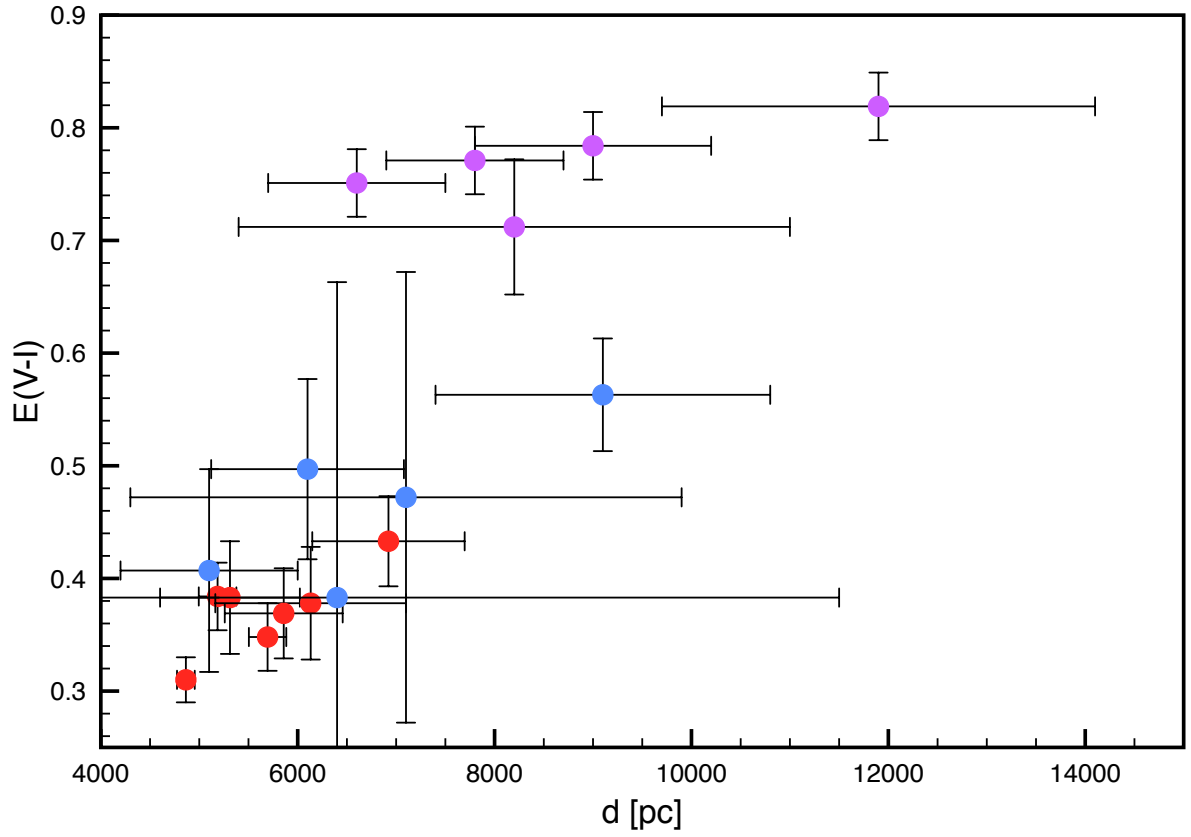


Fig. 10.— Spectroscopic results of reddening as a function of distance for the targets in Box C and D. The blue, violet, and red dots indicate the C1, C2, and D groups, respectively.

Fig. 10. Two stars slightly depart from this relation, probably due to differential reddening in the field of view. The shape of this sequence and its width are comparable with the ones found in the background of NGC 2354 (Carraro et al. 2016), or in the direction of the Canis Major over density (Carraro et al. 2008), where these sequences are ascribed to the warped old thin disk, that the line of sight intersects, thus producing the effect of probing a structure confined in distance.

The weighted average RV is $\sim 107 \text{ km s}^{-1}$, much higher than the expectation of a simple Galactic rotation model ($\approx 60 \text{ km s}^{-1}$) such as that presented by Moni Bidin et al. (2014). However, the model could easily fail at these large distances from the Galactic center, and far away from the formal Galactic plane (at latitude 0° deg). The line-of-sight velocity at this Galactic longitude mostly reflects the Galactocentric U component. The RV dispersion, after quadratic subtraction of the mean observational error, is $\sigma_{RV} = 23 \text{ km s}^{-1}$. This is very high, because $\sigma_U \approx 10 \text{ km s}^{-1}$ for the thin disk at the solar position, and the dispersion is expected to exponentially decline outwards. Hence, this intermediate-age and distant population presents peculiar kinematical properties. A possible explanation for this peculiarity is that this population belongs to the Galactic warp (Mormann et al. 2006), and it is also flared (see Carraro et al. 2015, and references therein). In this scenario the kinematics is not easily predictable (see Xu et al. 2015), since the outer disk exhibits several rings and waves, which alter the expected kinematics.

We now continue discussing stars in box C. These stars form a sequence which lies along the prolongation of the thick MS we just described. In this case they can be interpreted as blue straggler stars of this intermediate-age population. Their color and magnitude can also be compatible with them being thick disk or halo foreground hot sdBs, although we do not expect so many stars of this type in such a limited volume (Carraro et al. 2015). The spectroscopic data we have analysed in this work help us to understand better the nature of these stars.

Reading through Table 9 one can infer that these C group stars are early type stars, confirming earlier findings (Carraro et al. 2016, and references therein) based on photometry only. Therefore we remark that the *blue plumes* routinely found in many different lines of sight in the third quadrant of the Milky Way (Moitinho et al. 2006) are indeed sequences of young stars. Only one of the observed targets is likely a sdB star, as commented in Sect. 4.3 and it will be excluded from further discussion. For this specific line of sight, a quick glance at the CMDs in Fig. 1, 4, and 11 reveals that the stars selected for, and observed with, spectroscopy are clearly separated in the CMD, where there are five stars with $(V - I) < 0.57$ (hereafter C1 group) and five object at $(V - I) > 0.65$ (hereafter C2). The two groups seem to trace two separated sequences. The same dichotomy is found in the spectroscopic results. All C2 objects have $T_{eff} > 10\,000 \text{ K}$, while four of the five C1 stars are cooler than $10\,000 \text{ K}$. Thus, C2 stars are on average hotter, despite they are redder in the CMD, and in fact they exhibit a much larger reddening ($\overline{E(V - I)} = 0.46$ and 0.77 , for C1 and C2 groups, respectively).

The two groups also show a different behavior in the distance-reddening relation shown in Fig. 10. In fact, C1 stars are compatible with the distance-reddening relationship defined by box D

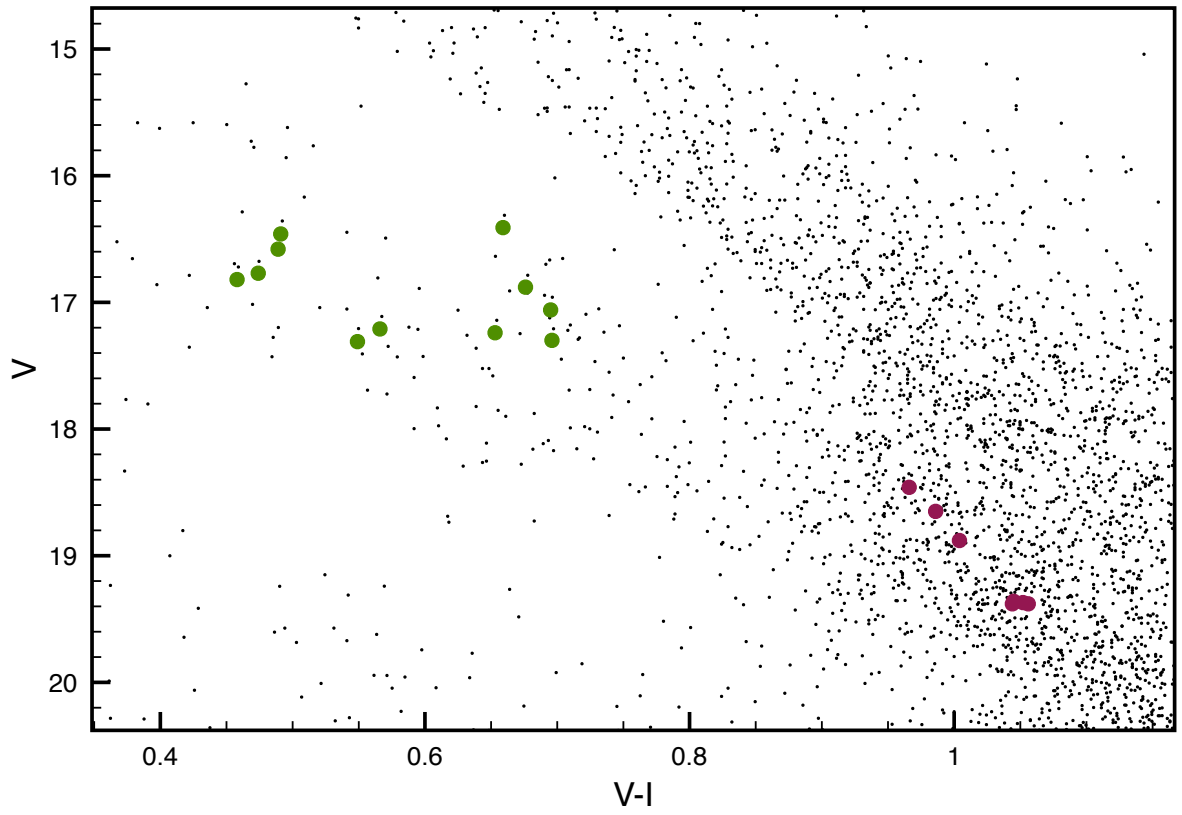


Fig. 11.— CMD of the field, with box C and box D targets marked with green and red symbols, respectively.

targets, and they are distributed in a distance range that largely overlaps that of box D stars, with a mean value of $d = 6.7$ kpc. C2 stars, on the other hand, are found at nearly constant reddening, and on average at a larger distance than box D and C1 stars ($d = 8.2$ kpc on average). In addition, the kinematics of the two C-groups also seems different. C1 stars are confined in a narrow range of RVs between 75 and 100 km s⁻¹, with a mean value of 91 km s⁻¹, similar to that found in box D. The mean RV of C2 stars, on the other hand, is 70 km s⁻¹, matching within few km s⁻¹ the expectations of a simple Galactic rotation model at $d = 8$ kpc. Their RV dispersion is also low, 8.2 km s⁻¹, as expected for a thin disk population.

The observed differences between C1 and C2 stars could be partially due to differential reddening. In Fig. 12 we show the position of the targets in the Schlegel et al. (1998) reddening map. There is clearly a variation of reddening in the field, and the C1 (C2) stars tend to be found far from (close to) a local reddening maximum. However, a further inspection suggests that this cannot fully explain the observed dichotomy. First, there is a certain degree of mixing in the spatial distribution, with a C2 target found in a low-reddening area and the object closest to the reddening maximum being a C1 star. In addition, the reddening variations are small in the Schlegel et al. (1998) map, where it varies by no more than 0.1 mag in the field under investigation. This is only one third of the difference between the average reddening of C1 and C2 groups. The variation would be even reduced if corrections to the maps, such as that proposed by Bonifacio et al. (2000), were applied. The differential reddening also cannot explain the different kinematics of the two groups, nor the distance-reddening relation observed for C1 and D stars. Moreover, spatial reddening variations alone would cause that more reddened stars are closer, contrary to what observed, because the targets in each box were selected photometrically at approximately the same magnitude. We conclude that differential reddening may play a role, but it cannot alone explain the observed differences between C1 and C2 groups.

We have to take these differences with a lot of care, since they are derived from a handful of stars. From the photometric analysis in fact we see a continuum of reddening and distance properties, where these two groups, C1 and C2, are representing the extremes of these young population, as seen from the CMD in Fig. 11. This discrepancy between the photometric and spectroscopic distribution of reddening and distances in Box C can offer two alternative interpretations: *i*) the distribution is broad and continuum, as indicated by the photometric results, and the spectroscopic dichotomy is only an spurious effect due to the random selection a small sample of targets, or due to selection biases; *ii*) The underlying distribution is bimodal, as the spectroscopic results suggest, but its nature is lost in the photometric results due to large uncertainties, which blend the two groups into a wider single peak. To investigate this issue in more details, we compare in Fig. 13 the distribution of $E(V - I)$ obtained with the spectroscopic and photometric method, for the same ten targets of the spectroscopic study. The histogram shows that the bimodal distribution found with the first method is completely lost when the photometrically-derived reddening are studied. This results suggests that, if the C1 and C2 groups represent two distinct stellar populations with different distances and reddening in the same field of view, their presence would have likely been

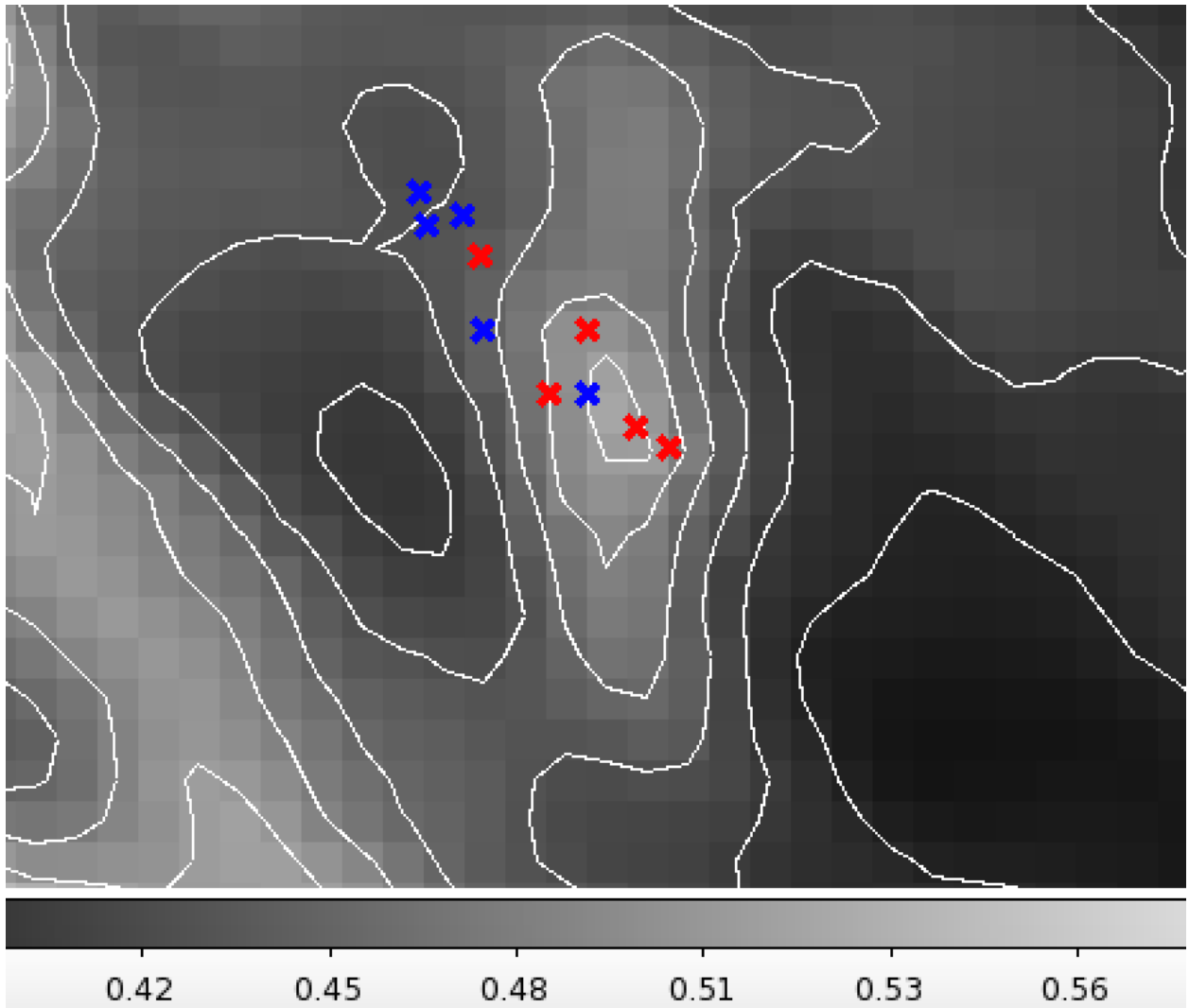


Fig. 12.— A reddening map from Schlegel et al (1998) in the region of Tombaugh 1. Blue and red crosses indicate stars from C1 and C2 sub-groups, respectively.

missed in the photometric results. A Kolmogorov-Smirnov test indicates that the probability that the bimodal spectroscopic results are randomly drawn from the photometric broad distribution is only 8%. Hence, the hypothesis that this multi-modality is entirely due to the random selection of a small sample of stars cannot be dismissed, but it is very improbable. However, while these tests tend to exclude the hypothesis *i*) above, they are insufficient to claim the existence of two stellar sub-structures at different distances in this field, both because of the too small spectroscopic sample, and because selection effects unaccounted for in the analysis could have led to a observed sample unevenly distributed in the CMD, thus giving the wrong impression of a bimodal distribution. A more extensive spectroscopic study of a larger sample of stars is required to fix this issue.

This young population is the very same that we found in several other direction in the third Galactic quadrant. It is confined in distance, being at heliocentric distances in the range 6 to 9 kpc. Within the uncertainties involved, these stars are most probably tracing a portion of the outer, or Norma-Cygnus, spiral arm. This arm is located well below the formal Galactic plane (at $b = 0^\circ$), because of the warp, and the line of sight to Tombaugh 1 intersects it, in close similarity to the line of sight to the old open cluster Auner 1 (Carraro et al. 2007). Being the Norma-Cygnus arm the outermost arm known for the Milky Way, it is not unexpected to find stars at so very different distances, because outermost arms are typically wider than inner disk arms, whose width is typically about 1 kpc. Interestingly, the line of sight to Tombaugh 1 does not contain young stars closer to the Sun (at 1.5–2.5 kpc), that we would expect from the crossing of the Perseus arm, which would be located at about 2 kpc from the Sun (Churchwell et al. 2009). The fact that we miss the Perseus arm means either that the warping of the disk starts to be significant beyond 2-3 kpc, or that the Perseus arm is not important in the third Galactic quadrant.

Finally, we comment on the stars located in the Box B. This box samples red giant stars. According to our results (see Tables 3 and 4), these stars, which seem to somehow group together in the CMD, are located at different distances, and have different metallicities. Thus, the stars of box B have no close relation to the populations of the box C and D. As discussed in Sect. 1, the presence of a background MS and a *blue plume* of hot young stars in the third Galactic quadrant have been interpreted as evidence of the recent accretion of the Canis Major satellite. We argued in Sect. 5 that we find no evidence of an extragalactic origin for any of our red clump targets. Unfortunately, the lack of a kinematical or spatial link of box B stars with the fainter box C and D groups, prevents us to extend the result to these features. However, red clump stars should be present in a complex stellar population as that postulated for the Canis Major satellite, and our sample included targets in a wide range of distance. Our results therefore favours the scenario where the peculiar features observed in the CMD are due to a complex mix of Galactic populations rather than the imprint of an extragalactic system.

We can divide the stars of box B in two field populations. The first composed by older stars, with ages of 8 Myr and 10 Gyr, belonging to the thick and thin disk (with slight majority for the thick disk) and a distance between $1.2 \leq d \leq 5.3$ kpc. The second population composed by young

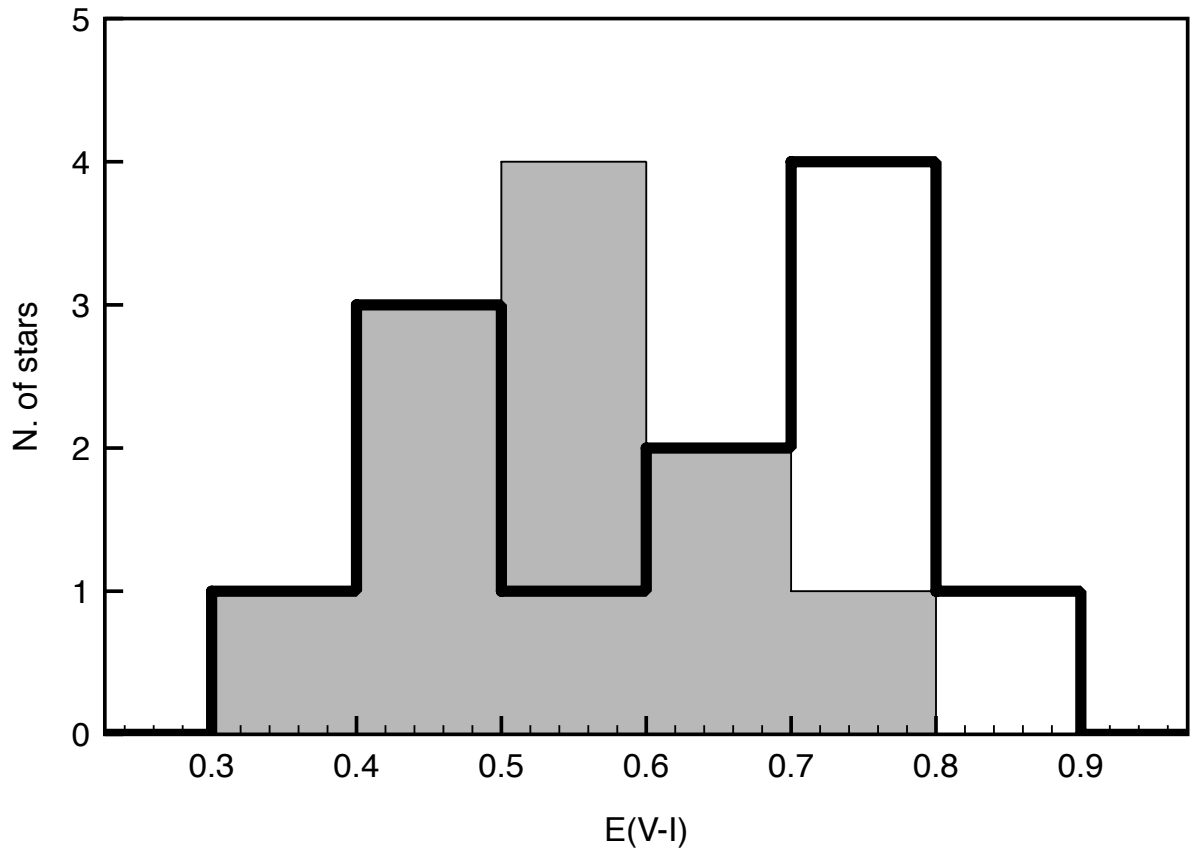


Fig. 13.— Histogram of the spectroscopic (thick black line) and photometric (shaded grey area)reddening distribution of the box C stars.

($\lesssim 8$ Myr) background field stars, with high values for distances ($d > 12$ kpc) and slightly similar radial velocities, with mean RV of 69 km s^{-1} . It is important to note that the distances to these background stars of the box B have large uncertainties with average of ~ 9 kpc being the important result for these stars that they are background stars relating the other stars of B box. It is worth mentioning that the detection of stars with large estimates of the distances, and consequently with large distance from the galactic plane, as the stars #13964, #28064, and #31364 in box B, and also apparently young when compared to thick disk stars and halo, is not expected, and can reveal an interesting and complex galaxy evolution occurring in the periphery of the warped and flared outer disk with a probable interaction with the Galactic halo. A contributing to this discussion comes from recent Galactic disk simulations reveal that younger populations have increasingly larger scale-lengths at larger distances from the galactic center Minchev et al. (2015). Such featured reveals the need for further analysis with a large sample of stars in this extreme region of the disk. The Gaia-ESO survey can help us to answer these questions better, since this survey will enable a reliable determination of the distances of large samples of these stars.

We express our deepest gratitude to Edgardo Costa, who acquired part of the data used for this work. Extensive use was made of the WEBDA database maintained by E. Paunzen at the University of Vienna, Austria (<http://www.univie.ac.at/webda>). J.V.S.S. acknowledges the support provided by CNPq/Brazil Science without Borders program (project No. 249122/2013-8). C.M.B. acknowledges support by the Fondo Nacional de Investigación Científica y Tecnológica (Fondecyt), project No. 1150060.

REFERENCES

- Alonso, A., Arribas, S., Martínez-Roger, C., 1999, *A&AS*, 140, 261
- Arnould, M., & Mowlavi, N. 1995, *Liege International Astrophysical Colloquia*, 32, 17
- Asplund, M., Grevesse, N., Sauval, A. J., & Scott, P. 2009, *ARA&A*, 47, 481
- Bellazzini, M., Ibata, R., Monaco, L., Martin, N., Irwin, M. J. & Lewis, G. F. 2004, *MNRAS*, 354, 1263
- Bensby, T., Feltzing, S., Lundström, I., & Ilyin, I. 2005, *A&A*, 433, 185
- Bensby, T., Alves-Brito, A., Oey, M. S., Yong, D., & Meléndez, J. 2011, *ApJ*, 735, L46
- Bensby, T., Feltzing, S., & Oey, M. S. 2014, *A&A*, 562, A71
- Bergeron, P., Saffer, R. A., & Liebert, J. 1992, *ApJ*, 394, 228
- Bertelli, G., Girardi, L., Marigo, P., Nasi, E. 2008, *A&A*, 484, 815

- Bertelli, G., Nasi, E., Girardi, L., Marigo, P. 2009, *A&A*, 508, 355
- Bessell, M. S., Castelli, F., & Plez, B. 1998, *A&A*, 333, 231
- Bienaymé, O., Famaey, B., Siebert, A., et al. 2014, *A&A*, 571, 92
- Blackwell, D. E., Booth, A. J., Menon, S. L. R., & Petford, A. D. 1986, *MNRAS*, 220, 289
- Bonifacio, P., Monai, S., & Beers, T. C. 2000, *AJ*, 120, 2065
- Carney, B. W., Yong, D., Teixeira de Almeida, M. L., & Seitzer, P. 2005, *AJ*, 130, 1111
- Carraro, G., Vázquez, R. A., Moitinho, A., & Baume, G. 2005, *ApJ*, 630, L153
- Carraro, G., Moitinho, A., Zoccali, M., Vazquez, R., Baume, G., 2007, *AJ*, 133, 1058
- Carraro, G., Moitinho, A., & Vázquez, R. A. 2008, *MNRAS*, 385, 1597
- Carraro, G., Vázquez, R. A., Costa, E., Perren, G., & Moitinho, A. 2010, *ApJ*, 718, 683
- Carraro, G., Monaco, L., Villanova, S., 2014a, *A&A*, 568, 86
- Carraro, G., Villanova, S., Monaco, L., Beccari, G., Ahumada, J., Boffin, H., 2014b, *A&A*, 562, 39
- Carraro, G., Vázquez, R. A., Costa, E., Ahumada, J. A., & Giorgi, E. E. 2015, *AJ*, 149, 12
- Carraro, G., Seleznev, A. F., Baume, G., & Turner, D. G. 2016, *MNRAS*, 455, 4031
- Carretta, E., Bragaglia, A., Gratton, R. G., & Tosi, M. 2004, *A&A*, 422, 951
- Carretta, E., Bragaglia, A., & Gratton, R. G. 2007, *A&A*, 473, 129
- Castro, S., Rich, R. M., Grenon, M., Barbuy, B., & McCarthy, J. K. 1997, *AJ*, 114, 376
- Charbonnel, C., & Lagarde, N. 2010, *A&A*, 522, A10
- Churchwell, E., Babler, B. L., Meade, M. R., Whitney, B. A., Benjamin, R., et al., 2009, *PASP*, 121, 213
- Coelho, P., Barbuy, B., Meléndez, J., Schiavon, R. P., & Castilho, B. V. 2005, *A&A*, 443, 735
- Denisenkov, P. A., & Denisenkova, S. N. 1990, *SvAL*, 16, 275
- Depagne, E., Hill, V., Spite, M., et al. 2002, *A&A*, 390, 187
- Drake, J. J., & Smith, G. 1991, *MNRAS*, 250, 89
- Dressler, A., Hare, T., Bigelow, B. C., & Osip, D. J. 2006, *Proc. SPIE*, 6269, 62690
- Edvardsson, B., Andersen, J., Gustafsson, B., Lambert, D. L., Nissen, P. E., & Tomkin, J. 1993, *A&A*, 275, 101

- Fuhrmann, K., Axer, M., & Gehren, T. 1994, *A&A*, 285, 585
- Genovali, K., Lemasle, B., da Silva, R., et al. 2015, *A&A*, 580, A17
- Gratton, R. G., & Sneden, C. 1988, *A&A*, 204, 193
- Gratton, R. G., Carretta, E., Eriksson, K., & Gustafsson, B. 1999, *A&A*, 350, 955
- Grevesse, N., & Sauval, A. J. 1998, *SSRv*, 85, 161
- Hawkins, K., Jofré, P., Masseron, T., & Gilmore, G. 2015, *MNRAS*, 453, 758
- Horne, K. 1986, *PASP*, 98, 609
- Katime Santrich, O. J., Pereira, C. B., & de Castro, D. B. 2013, *AJ*, 146, 39
- Keeping, E. S. 1962, *Introduction to Statistical Inference* (London: Van Nostrand)
- Kuijken, K., & Gilmore, G. 1989, *MNRAS*, 239, 605
- Kurucz, R. 1993, *ATLAS9 Stellar Atmosphere Programs and 2 km/s grid*. Kurucz CD-ROM No. 13. Cambridge, Mass.: Smithsonian Astrophysical Observatory, 1993, 13
- Lambert, D. L., Heath, J. E., Lemke, M., & Drake, J. 1996, *ApJS*, 103, 183
- Landolt, A. U. 1992, *AJ*, 104, 372
- Lee, Y.-W., Joo, S.-J., & Chung, C. 2015, *MNRAS*, 453, 3906
- Lemasle, B., François, P., Genovali, K., et al. 2013, *A&A*, 558, 31
- Letarte, B., Hill, V., Jablonka, P., Tolstoy, E., François, P., & Meylan, G. 2006, *A&A*, 453, 547
- Lind, K., Asplund, M., Barklem, P. S., & Belyaev, A. K. 2011, *A&A*, 528, A103
- Magrini, L., Sestito, P., Randich, S., & Galli, D. 2009, *A&A*, 494, 95
- Magrini, L., Randich, S., Zoccali, M., Jilková, L., Carraro, G., et al., 2010, *A&A*, 523, 11
- Magrini, L., Randich, S., Romano, D., Friel, E.D., et al., 2014, *A&A*, 563, 44
- Majaess, D., Carraro, G., Moni Bidin, C., et al. 2013, *A&A*, 560, A22
- Martin, W. C., Fuhr, J. R., Kelleher, D. E., et al. 2002, *NIST Atomic Spectra Database* (Version 2.0; Gaithersburg, MD: NIST)
- Martin, N. F., Ibata, R. A., Bellazzini, M., et al. 2004, *MNRAS*, 348, 12
- Masseron, T., & Gilmore, G. 2015, *MNRAS*, 453, 1855

- McWilliam, A., & Rich, R. M. 1994, *ApJS*, 91, 749
- Minchev, I., Martig, M., Streich, D., et al. 2015, *ApJ*, 804, L9
- Mishenina, T., Pignatari, M., Carraro, G., et al. 2015, *MNRAS*, 446, 3651
- , Moitinho, A., 2001, *A&A*, 370, 436
- Moitinho, A., Vázquez, R. A., Carraro, G., Baume, G., Giorgi, E. E., & Lyra, W. 2006, *MNRAS*, 368, 77
- Momany, Y., Zaggia, S., Gilmore, G., et al. 2006, *A&A*, 451, 515
- Moni Bidin, C., de la Fuente Marcos, R., de la Fuente Marcos, C., & Carraro, G. 2010, *A&A*, 510, A44
- Moni Bidin, C., Villanova, S., Piotto, G., & Momany, Y. 2011b, *A&A*, 528, A127
- Moni Bidin, C., Carraro, G., & Méndez, R.A. 2012, *ApJ*, 747, 101
- Moni Bidin, C., Villanova, S., Piotto, G., Moehler, S., Cassisi, S., & Momany, Y. 2012, *A&A*, 547, A109
- Moni Bidin, C., Majaess, D., Bonatto, C., et al. 2014, *A&A*, 561, 119
- Morse, J.A., Mathieu, R.D., & Levine, S.E. 1991, *AJ*, 101, 1495
- Munari, U., Sordo, R., Castelli, F., & Zwitter, T. 2005, *A&A*, 442, 1127
- Napiwotzki, R., Green, P. J., & Saffer, R. A. 1999, *ApJ*, 517, 399
- Nieva, M. F., & Przybilla, N. 2007, *A&A*, 467, 295
- Pasquini, L., Randich, S., Zoccali, M., et al. 2004, *A&A*, 424, 951
- Patat, F., & Carraro, G. 2001, *MNRAS*, 325, 1591
- Pereira, C. B., Sales Silva, J. V., Chavero, C., Roig, F., & Jilinski, E. 2011, *A&A*, 533, A51
- Preston, G. W., & Sneden, C. 2001, *AJ*, 122, 1545
- Reddy, B. E., Bakker, E. J., & Hrivnak, B. J. 1999, *ApJ*, 524, 831
- Reddy, B. E., Tomkin, J., Lambert, D. L., & Allende Prieto, C. 2003, *MNRAS*, 340, 304
- Reddy, A. B. S., Giridhar, S., & Lambert, D. L. 2013, *MNRAS*, 431, 3338
- Romero-Gómez, M., Figueras, F., Antoja, T., Abedi, H., & Aguilar, L. 2015, *MNRAS*, 447, 218
- Saffer, R. A., Bergeron, P., Koester, D., & Liebert, J. 1994, *ApJ*, 432, 351

- Sales Silva, J.V., Carraro, G., Anthony-Twarog, B.J., Moni Bidin, C., Costa, E., & Twarog, B.A. 2016, *AJ*, 151, 6
- Santrich, O. J. K., Pereira, C. B., & Drake, N. A. 2013, *A&A*, 554, A2
- Sbordone, L., Bonifacio, P., Marconi, G., Zaggia, S., & Buonanno, R. 2005, *A&A*, 430, L13
- Sbordone, L., Bonifacio, P., Buonanno, R., Marconi, G., Monaco, L., & Zaggia, S. 2007, *A&A*, 465, 815
- Sbordone, L., Monaco, L., Moni Bidin, C., et al. 2015, *A&A*, 579, 104
- Schlegel, D. J., Finkbeiner, D. P., & Davis, M. 1998, *ApJ*, 500, 525
- Snedden, C. 1973, *ApJ*, 184, 839
- Snedden, C., Ivans, I. I., & Fulbright, J. P. 2004, in *Origin and Evolution of the Elements*, 17
- Tonry, J., & Davis, M. 1979, *AJ*, 84, 1511
- Turner, D. G., 1976, *AJ*, 81, 97
- Turner, D.G., 1979, *PASP*, 91, 642
- Turner, D. G., 1983, *JRASC*, 77, 31
- Turner, D. G., MacLellan, R. F., Henden, A. A., & Bernikov, L. N. 2011, *RMxAA*, 47, 345
- Turner, D. G., Majaess, D. J., & Balam, D. D. 2011, *CJP*, 92, 1696
- van Dokkum, P. G. 2001, *PASP*, 113, 1420
- Vazquez, R.A., May, J., Carraro, G., Bronfman, L., Moitinho, A., Baume, G., 2008, *ApJ*, 672, 930
- Wan, J.-C., Liu, C., Deng, L.-C., et al. 2015, *Research in Astronomy and Astrophysics*, 15, 1166
- Wiese, W. L., Smith, M. W., & Miles, B. M. 1969, *NSRDS-NBS*, Washington, D.C.: US Department of Commerce, National Bureau of Standards, 1969
- Woosley, S. E., & Weaver, T. A. 1995, *ApJS*, 101, 181
- Xu, Y., Newberg, H. J., Carlin, J. L., et al. 2015, *ApJ*, 801, 105
- Yong, D., Carney, B. W., Teixeira de Almeida, M. L., & Pohl, B. L. 2006, *AJ*, 131, 2256
- Yong, D., Carney, B. W., Teixeira de Almeida, M. L., & Pohl, B. L. 2006, *AJ*, 131, 2256